

AD-A032 757

CALIFORNIA UNIV LIVERMORE LAWRENCE LIVERMORE LAB
BEHAVIOR OF POROUS BERYLLIUM UNDER THERMOMECHANICAL LOADING. PA--ETC(U)
NOV 74 F H REE, W M ISBELL, R R HORNING W-7405-ENG-48

UNCLASSIFIED

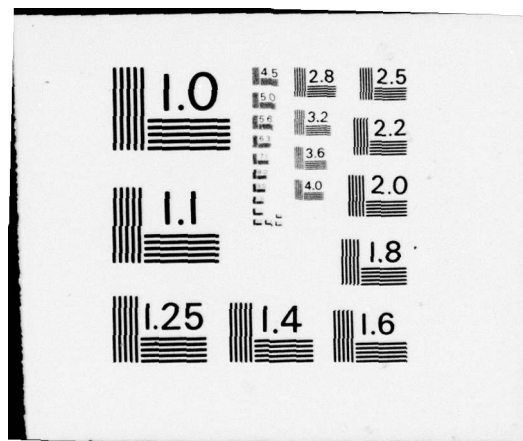
UCRL-51682-PT-4

F/G 11/6

NL

1 OF 1
ADA032757





AD A 032757

Good pt.

1 NW
14 UCRL-51682-Pt. 4

6
**BEHAVIOR OF POROUS BERYLLIUM UNDER
THERMOMECHANICAL LOADING.
PART 4. CONSTITUTIVE MODEL FOR WAVE PROPAGATION,**

10 Francis H./Ree,
W. M./Isbell
R. R./Horning

11 5 Nov 74

November 5, 1974

12 46p.

15
Prepared for U.S. Atomic Energy Commission under contract No. W-7405-Eng-48



**LAWRENCE
LIVERMORE
LABORATORY**

University of California/Livermore

DDC
RECEIVED
DEC 2 1976
RECEIVED

390 999 AB J A

DISTRIBUTION STATEMENT A
Approved for public release;
Distribution Unlimited

NOTICE

"This report was prepared as an account of work sponsored by the United States Government. Neither the United States nor the United States Energy Research & Development Administration, nor any of their employees, nor any of their contractors, subcontractors, or their employees, makes any warranty, express or implied, or assumes any legal liability or responsibility for the accuracy, completeness or usefulness of any information, apparatus, product or process disclosed, or represents that its use would not infringe privately-owned rights."

Printed in the United States of America
Available from
National Technical Information Service
U. S. Department of Commerce
5285 Port Royal Road
Springfield, Virginia 22151
Price: Printed Copy \$ ____*; Microfiche \$2.25

<u>*Pages</u>	<u>NTIS Selling Price</u>
1-50	\$4.00
51-150	\$5.45
151-325	\$7.60
326-500	\$10.60
501-1000	\$13.60

TID-4500, UC-34 ✓
Physics - General



LAWRENCE LIVERMORE LABORATORY ✓
University of California / Livermore, California / 94550

UCRL-51682 Pt. 4 ✓

**BEHAVIOR OF POROUS BERYLLIUM UNDER
THERMOMECHANICAL LOADING:
PART 4. CONSTITUTIVE MODEL FOR WAVE PROPAGATION**

Francis H. Ree

W. M. Isbell

R. R. Horning

MS. date: November 5, 1974

Preface

This report is Part 4 of a seven-part series on Behavior of Porous Beryllium Under Thermomechanical Loading (UCRL-51682 Pts. 1-7). The titles and authors of the individual reports in the series are as follows:

Title	Author
Part 1. Summary of Results	W. M. Isbell
Part 2. Quasi-Static Deformation	R. N. Schock, A. E. Abey, and A. G. Duba
Part 3. Shock Wave Studies	W. M. Isbell and R. R. Horning
Part 4. Constitutive Model for Wave Propagation	F. H. Ree, W. M. Isbell, and R. R. Horning
Part 5. Electron-Beam Studies	O. R. Walton and W. M. Isbell
Part 6. Effect of Pressure on the Micro-structure of Plasma-Sprayed Beryllium	J. E. Hanafée and E. O. Snell
Part 7. Calibration Studies on the Carbon Piezoresistive Gage	R. R. Horning and W. M. Isbell

This work was supported by the Defense Nuclear Agency (Mr. Donald Kohler, technical monitor) under the auspices of the U.S. Atomic Energy Commission.

Contents

Abstract	1
1. Introduction	1
2. Characterization of Porous Beryllium	4
2.1 Structural Characteristics	4
2.2 Static Deformation Characteristics	5
2.3 Ultrasonic Velocities	7
2.4 Shock Wave Characteristics	7
3. Description of the Porous Constitutive Model	13
3.1 First Constitutive Relation: EOS of Porous Materials	13
3.2 Second Constitutive Relation: Equation for the Porosity Parameter	14
3.2.1 Plastic Path	14
3.2.2 Elastic Path	15
3.3 Yield Stress	17
4. Computational Procedure	19
5. Comparison Between Predicted and Experimental Wave Profiles	22
5.1 Compressional Waves	25
5.2 Gage Effect	31
5.3 Release Wave	34
5.4 Other Remarks	35
6. Conclusions	41
Acknowledgments	41
References	42

ADDITIONAL TO:	
RTTS	Write Section <input checked="" type="checkbox"/>
DPC	Data Section <input type="checkbox"/>
TRANSLATIONS	<input type="checkbox"/>
INSTRUCTIONS	
<i>Letter on file</i>	
BY	
DISTRIBUTION/AVAILABILITY CODE	
DINT.	AVAIL. NO. OF SPECIAL
A	

BEHAVIOR OF POROUS BERYLLIUM UNDER THERMOMECHANICAL LOADING:

PART 4. CONSTITUTIVE MODEL FOR WAVE PROPAGATION

Abstract

↓
A new constitutive model for wave propagation in porous materials is constructed here. Based on similar models proposed earlier by Herrmann and Holt, the new model features (1) inclusion of deviatoric stresses, (2) an option for porosity-dependent relaxation time for pore closure, (3) elastic reopening of the pores, and (4) an improved plastic compaction function.

This model has been applied to plasma-sprayed porous beryllium in the as-sprayed condition (~14% porosity) and after sintering (~10% porosity). We discuss techniques used to correlate data from the static and dynamic experiments

which were conducted to provide the supporting inputs to the model. Wave profiles generated from plate impact experiments were used to test the model under different experimental conditions. The resulting good agreement between the model calculations and wave profile experiments suggests that the mechanical response of porous beryllium can be satisfactorily described within the necessary accuracy by this model. We also discuss two other relevant topics, namely, the effect of an in-material gage on observed wave profiles, and a transient phenomenon affecting the wave profile at the impact surface.

are discussed.

** approx.*

1. Introduction

When a thin plate impacts at high velocity against a metal target, it generates a stress pulse which travels through the target medium. Response to the stress wave is slightly more complicated when the medium is porous. First we note that the compressive side of the pulse travels with much lower velocity in the porous medium than in the corresponding solid medium. In the case of 10% porous plasma-sprayed sintered beryllium, for example, a 2-GPa (= 20-kbar) stress wave

attains a speed of 0.35 cm/ μ s, which represents only 42% of the shock speed of solid beryllium. This dramatic decrease in shock wave velocity is a common occurrence in most porous metals and is associated with the extra time taken by the shock wave either in closing the pores or in being scattered from them. The second notable feature occurs on the release side of the pulse. Experiments on the release wave velocities in porous aluminum and beryllium¹⁻³ have shown

that these velocities depend less sensitively on initial porosity and lie closer to release wave velocities in corresponding nonporous samples. A 2-GPa stress wave in 10% porous sintered beryllium quoted in the above example has an initial release wave speed of 1.3 cm/ μ s. This is nearly the same as the release wave speed of solid beryllium. Both of these features imply that reopening of the pores does not take place to a large extent and that the pore closure achieved during compaction is primarily accomplished by a plastic flow process.

The large difference between the compressive and release wave velocities shows up more dramatically in the attenuation of a stress pulse. The pulse attenuates very rapidly after propagating a relatively short distance through the porous medium. This immediately suggests a useful application. Namely, a thin layer of porous material, coated over a solid substructure, can be used to protect the substructure against high-intensity, short-duration shock waves arising from either mechanical impact or other types of rapid energy deposition (e.g., sudden heating).

For such applications, it is essential to carry out computer simulations using a physical model that can accurately predict the dynamic behavior of porous materials. The present work is addressed to this problem.

As a representative material for the porous metals we have chosen porous beryllium, whose dynamic response is porosity-dependent up to stress levels as high as 4 GPa. Beryllium remains porous over a relatively large range of pressure, which makes it useful for

testing the model at different stress levels. Two plasma-sprayed varieties were considered in our modeling effort — an "as-sprayed" beryllium with a nominal density of 86%, and a "sintered" beryllium which was densified to 90% of solid density by a sintering process. Experimental evidence described later indicates that the two porous beryllium specimens show different compaction and release behaviors. These features were incorporated in our model.

A combined theoretical and experimental study was performed in which structural characterization of the porous beryllium by photomicrography, static stress-strain testing, and ultrasonic data provided information essential for formulating and calibrating the model, while plate impact tests were conducted to check the predictive capabilities of the model. These experiments have been carried out at this Laboratory, and some of them have been reported separately and are the subjects of other reports in this series.³⁻⁷

Our model is based on the P - α - τ model of Holt et al.,⁸ which is a rate-dependent modification of the P - α model developed by Herrmann.⁹ The porosity parameter α , which is the ratio of the porous to solid volumes, and the relaxation time τ , which is the time necessary for the pores to close to a final equilibrium size, play important roles in these models. These models develop a simple constitutive relation between the pressure and α . Thus the difficult task of developing a complicated relation connecting the pressure, volume, and energy of a porous material is bypassed.

The difference in the compressive and release wave velocities noted earlier is

attributed in our model to the change in the porosity parameter α , while τ can account for some persuasive evidence (e.g., nonzero shock risetime, dispersion and attenuation of a precursor, and the possible presence of transient effects in the shock front when measurements are taken at the impact surface) that such rate-dependent effects are indeed present in experimentally measured wave profiles. Holt's and Herrmann's models are, however, hydrodynamic models. Therefore, they do not explain in a self-consistent manner any effect (such as an elastic-plastic nature of release wave profiles) originating from deviatoric stresses.

We added the deviatoric corrections to these models. This was done by using the porous bulk- and shear-modulus expressions derived from slightly generalizing Mackenzie's expressions¹⁰ which are applicable to a linear elastic medium containing spherical pores. These expressions (except for a slight modification) are the same as those proposed earlier by Seaman.¹¹ The present model also includes an improved static compaction function that was deduced from the hydrostatic measurements.

Sintered and as-sprayed beryllium behave differently, especially along initial loading portions. While the extended forms of Mackenzie's expressions are

suitable to describe the loading behavior of sintered porous beryllium, the same procedure cannot be used to describe the loading data of the as-sprayed porous beryllium. This is due to a relatively large number of nonspherical pores and irregularly shaped cracks which separate different beryllium grains in the as-sprayed material. For as-sprayed porous beryllium, therefore, we assume that the loading occurs plastically from the beginning of compaction. For this purpose, we introduce a porosity-dependent relaxation time τ whose expression was derived from a spherical model calculation for an elastic-viscoplastic material by Cristescu¹² and Holt et al.¹³ The use of such an expression gives a wave front which is sharply rising at the foot but later becomes dispersive at the peak, a behavior much in evidence in the wave profiles.

A computer program¹⁴ describing the model was included as a constitutive model in the one-dimensional hydrodynamic code KO¹⁵ and was applied to plate impact experiments, where accurate data on full and attenuated wave profiles were available. This comparison provides one of the severest tests of the model's adequacy. The satisfactory results described below lead us to believe that the mechanical response of porous beryllium can be described adequately by our model.

2. Characterization of Porous Beryllium

Our porous model requires information from several types of static and dynamic experiments on porous beryllium. These experiments were done on porous beryllium specimens from the same batches in all the test series to avoid the common problem in experiments on porous materials of batch-to-batch variations, thus assuring a consistent comparison between experiments and computations. Several groups at LLL contributed to this work: photomicrography and material characterization data was provided by Hanafee and Snell,⁴ quasi-static deformation data by Schock, Abey, and Duba,⁵ ultrasonic velocity measurements by Green,⁶ and Hugoniot and wave profiles by Isbell and Horning³ and Gust.⁷ Some of these data had to be reduced into forms applicable for model-building purposes. We give below an overview of the experimental results and discuss techniques used to correlate those features that are relevant to the present work.

2.1 STRUCTURAL CHARACTERISTICS

Beryllium powders supplied by Kawecki Berylco Industries were plasma-sprayed in a dry argon atmosphere onto a rotating aluminum mandrel, which was removed after the plasma spray. Thickness of the finished plate ranged from 0.48 to 0.55 cm across the radius. One specimen (designated as "sintered") was heat-treated 2 hours at 1175°C, while the other specimen (designated as "as-sprayed" and with a slightly different initial powder) had no such heat treatment. Chemical analysis showed that the as-sprayed and the sin-

tered Be plates contained about 1.5 wt% of BeO. The other impurities (Fe, Al, C, Mg, W) totaled 0.35% and 0.20% each for the as-sprayed and the sintered specimens.

A more complete description of the two materials, including spectrographic analyses, is given in Ref. 3. In the computations presented later, we use initial densities of 1.660 g/cm³ and 1.591 g/cm³ for the sintered and the as-sprayed Be specimens, respectively. These values agree, within the experimental uncertainties, with measurements.

Figure 1 shows photomicrographs of the sintered and as-sprayed samples. Comparison of the sintered and as-sprayed specimens shows that the pores in the as-sprayed specimen are more irregular in shape, larger in number, and have a wider size distribution. There are also cracklike structures in the as-sprayed material, formed by colonies of larger pores. Sintering, in addition to densifying the material by about 4%, reduces the number of pores and makes them less irregular in shape and more uniform in size. This difference is taken into account in our model.

In all test specimens, the outer 0.015-cm layer from the top and bottom sides of both sintered and as-sprayed machined specimens was removed by chemical etching. The densification of surface layers arises from the machining process and can lead to erroneous experimental results if not removed. Considerable twinning of the beryllium grains was noted in the densified layers, the effect being most predominant in the sintered material.

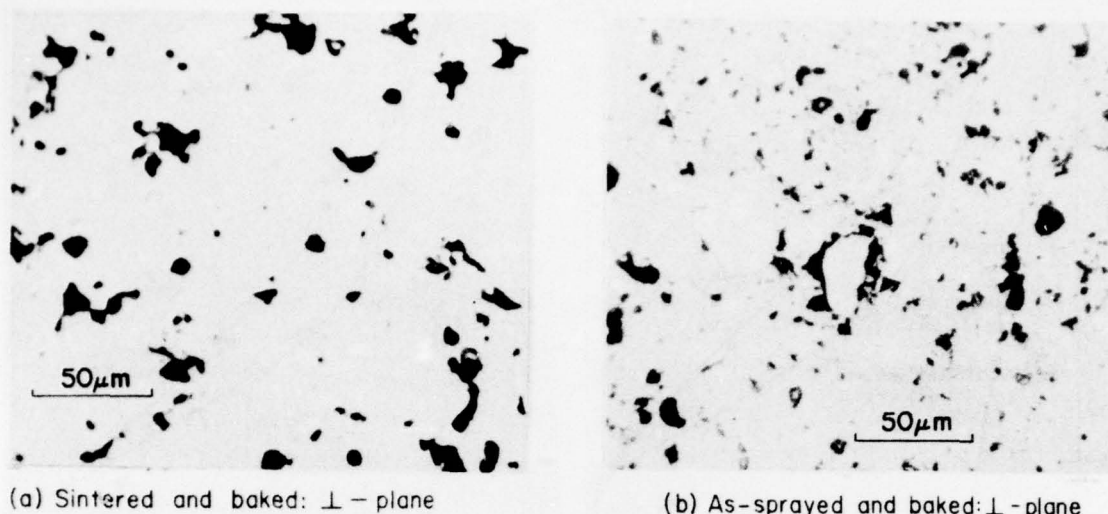


Fig. 1. Photomicrographs of plasma-sprayed porous beryllium: (a) sintered specimen, baked at 450°C, (b) as-sprayed specimens, baked at 450°C. These cross sections are normal to the direction of plasma spray. (Photographs taken by Hanafee and Snell, Ref. 4.)

2.2 STATIC DEFORMATION CHARACTERISTICS

Figure 2(a) shows the hydrostatic pressure-volume relation for the sintered beryllium. The portion of the hydrostat from 0 to 0.8 GPa was obtained under true hydrostatic conditions, in which a specimen was coated with semiflexible epoxy and fitted with foil strain gages to measure circumferential and axial strains. It was then placed in a pressure-transmitting fluid (oil), and the pressure-volume relationship was measured. Above 0.8 GPa the measurements were obtained by a "quasi-hydrostatic" method,¹⁶ in which the sample was surrounded by a pressure-transmitting medium (tin) and forces were applied to top and bottom by pistons. Tin, with its low yield strength, acts like a fluid for pressures above its yield stress (≤ 0.01 GPa). Note that the hydrostat exhibits an elastic yield at approximately 0.4 GPa. The slope of the porous hydrostat at the relatively high pressure of

4 GPa is only slightly less than that of the solid hydrostat,¹⁷ but a relatively large porosity (2.2%) still remains at this pressure. The residual porosity of about 2%, which appears to remain even under extremely compressed states,⁷ is taken into account in our model.

The hydrostat for as-sprayed beryllium given in Fig. 1 of Ref. 5 was obtained by using the quasi-hydrostatic data above 1.2 GPa and the hydrostatic data below 0.5 GPa. In the region between 1.2 and 0.5 GPa, which corresponds to a relatively large range in the volume strain, "interpolated" values were used to smoothly connect the lower and upper portions of the hydrostat. At pressures above 2.5 GPa the hydrostat for as-sprayed beryllium lies below that for sintered beryllium with a nearly constant volume offset of about $0.008 \text{ cm}^3/\text{g}$. Possible errors in the experimental system for quasi-static compaction include frictional forces that exist at interfaces

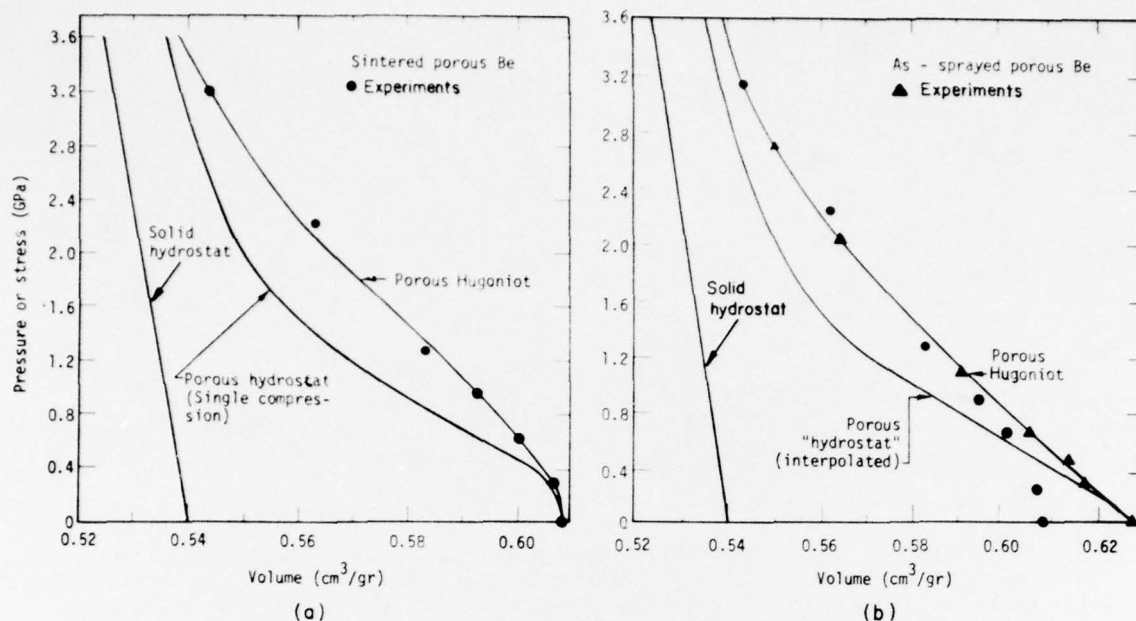


Fig. 2. Hydrostats and Hugoniot of porous and solid beryllium: (a) sintered and (b) as-sprayed specimens. Solid dots and triangles are experimental Hugoniot points of sintered and as-sprayed specimens, respectively. Hydrostat for sintered specimen is that of Schock et al.,^{5,16} while hydrostat for as-sprayed specimen is obtained by an interpolation scheme described in the text.

of the sample, the die, and the piston, and problems arising from the experimental necessity of stacking several layers of porous beryllium disks to make a specimen thick enough to test. Such errors are of a magnitude to account for the observed volume differences.

Therefore, for the calculations, we used a slightly different hydrostat (Fig. 2(b)) for as-sprayed beryllium, but one which is probably equally reliable. This was drawn using the following physical observations. First, we noted that the Hugoniot of both the sintered and the as-sprayed specimens shown in Fig. 2(b) are nearly equal to each other for stresses larger than about 1 GPa. This suggested to us that variations in the microstructure of beryllium are low-strength phenomena, and that they do not

affect the bulk properties at higher stresses. We concluded, therefore, that the hydrostats of both as-sprayed and sintered specimens would also be close to each other if the pressure exceeded a certain level, probably about 1 GPa. Additional insight was obtained from the ultrasonic measurements. The experiment which was conducted to detect a transmitted shear wave failed to do so because of the shear wave's small magnitude in the case of the as-sprayed specimen. Assuming that the specimen is isotropic, this implies that both the hydrostatic P-V data and the one-dimensional (1-D) strain data would likely have nearly equal initial slopes and hence come very close to each other at low stress levels. Our porous hydrostat in Fig. 2(b) is drawn to agree with these observations. That is, at pressures beyond 1.2 GPa it is forced to

agree with the porous hydrostat of the sintered specimen, and below 0.2 GPa it is forced to agree with the 1-D strain data. We should note, however, that porous plasma-sprayed beryllium is not perfectly isotropic at a low stress level. The hydrostat and the mean stress obtained from the 1-D strain tests do not coincide at a given volume strain, although the average of the two agrees with the axial stress obtained from 1-D strain tests at 0.2 GPa or less. At present, it is not clear how much the anisotropic correction would affect the wave profiles at low stress levels. We assume it negligible in our treatment. As will be seen later, wave profiles that were obtained under this assumption agree satisfactorily with experimental wave profiles.

Another static deformation experiment yielding information that we incorporated in the model was the cyclic unloading and reloading experiment under 1-D strain conditions. When porous samples were subjected to a cyclic loading-unloading-reloading stress with ever-increasing load after every cycle, the reloading portion of the stress-strain path returned very close to the original stress and strain levels where the unloading started. This feature was incorporated in our yield-strength expression.

2.3 ULTRASONIC VELOCITIES

The values of the sound velocities given below were taken in the direction perpendicular to the surface of the porous specimens. This is the same direction in which the plasma was sprayed in making the specimen material, and it is also the direction of stress wave propagation in our plate impact experiments.

	Ultrasonic velocity (cm/ μ s)	
	Longitudinal	Shear
Sintered Be	1.15	0.81
As-sprayed Be	0.34	$\sim 0^a$

^aToo small to be measured.

In the case of the sintered specimen, the longitudinal velocity was taken at 10 MHz and the shear velocity at 5 MHz. The values quoted above are the average values taken for two different thicknesses. Probable errors in these measurements are $\pm 2\%$. For the as-sprayed specimens a test of the frequency dependence of the longitudinal velocity was made at 5 MHz and 15 MHz, using two plates cut from the same specimen. The measured velocities at these frequencies were 0.343 and 0.338 cm/ μ s for the first plate, and 0.358 and 0.355 cm/ μ s for the second plate. This indicates no significant frequency dependence on the sound speed over the frequency range tested. Since the data on the two plates agree closely, we chose the values obtained from the first plate in our model. As we mentioned earlier, measurement of the shear-wave velocity was not successful. Its small magnitude was difficult to detect because of mode conversion, dispersion, and/or attenuation that resulted from interaction between the shear wave and the inhomogeneities in the porous specimen.

2.4 SHOCK WAVE CHARACTERISTICS

Three series of plate impact tests were conducted. The first series was designed to obtain Hugoniot data over the stress range 0 to 4 GPa, while the second series was used to measure profiles of

attenuated and unattenuated shock waves at different specimen thicknesses and different initial stresses. The third series of shock wave tests was conducted using high explosives to measure Hugoniot points to 33.5 GPa.^{3,7} Hugoniot points were needed to estimate the deviator contribution in the model, while shock wave profiles were used to check the adequacy of our model.

Figure 3(a) shows the impactor-target geometry used to measure Hugoniot points. Four porous specimens were mounted on the front of a projectile and impacted directly onto x-cut quartz piezoelectric gage assemblies on which four different buffers (PMMA, tantalum, x-cut quartz,

and fused quartz) with known Hugoniot points had been mounted. With this arrangement, the buffers not only reduced the noise on the gage signal coming from the abrasion of the front surface, but also, used as impedance-matching materials, allowed four different stresses to be obtained on a single shot.

In Table 1, the measured Hugoniot stress (σ_H) and particle velocity (U_p) data as well as the values of the volume and shock velocity (U_s) computed by using σ_H and U_p in Hugoniot relations are summarized for both the sintered and as-sprayed materials. In the calculation of U_s and V for the sintered material, we used the value of 0.2 GPa for the stress

Table 1. Experimental data and analytically fitted Hugoniot points for sintered and as-sprayed porous beryllium. U_p = particle velocity, U_s = shock velocity, σ_H = Hugoniot stress, and V = specific volume.

Experimental data for sintered porous Be				Analytic fit, Eq. (1a)	
U_p (cm/ μ s)	U_s (cm/ μ s)	σ_H (GPa)	V (cm ³ /g)	σ_H (GPa)	V (cm ³ /g)
0.00266	0.5071 ^a	0.338	0.6062 ^a	0.333	0.6059 ^a
0.00711	0.4561	0.678	0.6004	0.653	0.5997
0.01107	0.4372	0.922	0.5942	0.918	0.5939
0.01684	0.4186	1.234	0.5840	1.283	0.5848
0.03098	0.4017	2.216	0.5636	2.170	0.5623
0.04435	0.4190	3.144	0.5444	3.173	0.5448
0.05601	0.4598	4.350	0.5353	4.342	0.5349
Experimental data for as-sprayed porous Be				Analytic fit, Eq. (1b)	
U_p (cm/ μ s)	U_s (cm/ μ s)	σ_H (GPa)	V (cm ³ /g)	σ_H (GPa)	V (cm ³ /g)
0.00601	0.3050 ^a	0.277	0.6171 ^a	0.291	0.6177 ^a
0.01005	0.3161	0.525	0.6109	0.504	0.6101
0.0132	0.3230	0.680	0.6045	0.677	0.6044
0.0212	0.3568	1.11	0.5896	1.129	0.5903
0.0366	0.3518	2.06	0.5651	2.043	0.5645
0.0466	0.3667	2.69	0.5501	2.700	0.5504
0.0573	0.3978	3.62	0.5394	3.618	0.5394

^aThe Hugoniot relations are used to obtain these data. For sintered porous Be, we used a Hugoniot elastic limit $\sigma_{HEL} = 0.2$ GPa and $U_{HEL} = 1.15$ cm/ μ s.

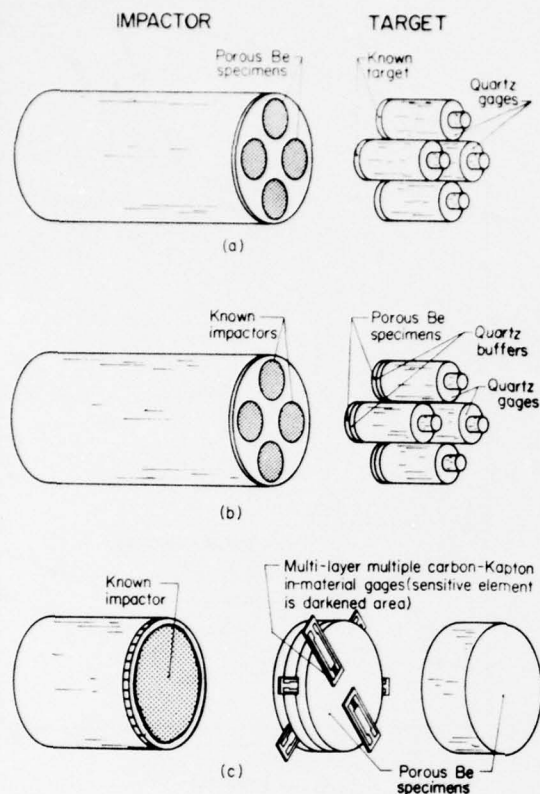


Fig. 3. Impactor-target geometries used to obtain (a) Hugoniot points, (b) transmitted wave profiles taken with quartz gages, and (c) wave profiles taken with in-material gages.

(σ_{HEL}) at the Hugoniot elastic limit with a velocity of $1.15 \text{ cm}/\mu\text{s}$ determined from the ultrasonic measurement. The σ_{H} -vs- U_{p} data were fitted with the polynomials in U_{p} (cm/ μs) given below:

Sintered Be

$$\begin{aligned} \sigma_{\text{H}} \text{ (GPa)} &= 0.1284 + 79.2U_{\text{p}} - 874U_{\text{p}}^2 \\ &\quad + 1.434 \times 10^4 U_{\text{p}}^3, \\ 0.3 &< \sigma_{\text{H}} \leq 4.5 \text{ GPa. (1a)} \end{aligned}$$

As-sprayed Be

$$\begin{aligned} \sigma_{\text{H}} \text{ (GPa)} &= 44.89U_{\text{p}} + 683.4U_{\text{p}}^2 \\ &\quad - 1.782 \times 10^4 U_{\text{p}}^3 \\ &\quad + 1.999 \times 10^5 U_{\text{p}}^4, \\ \sigma_{\text{H}} &\leq 4 \text{ GPa. (1b)} \end{aligned}$$

As shown in Fig. 4(a) and Table 1, these expressions give accurate representations of the experimental points. The deviations between the experimental points and the values calculated from Eq. (1) lie within the experimental uncertainties ($\pm 3\%$ in stress and $\pm 2\%$ in particle velocity).

Equation (1) was used to calculate σ_{H} vs V (Fig. 2) and U_{s} vs U_{p} (Fig. 4(b)). These calculations are not affected to a significant degree by the choice of $\sigma_{\text{HEL}} = 0.2 \text{ GPa}$. The HEL was measured as a function of distance of propagation and was seen to decrease from about 0.4 GPa at 0.1 cm to about $0.2\text{--}0.3 \text{ GPa}$ for distances greater than 0.3 cm . Figure 4(b) also shows theoretical longitudinal sound speeds that were calculated using Eq. (1b) and the bulk moduli of the porous beryllium specimens given in Sec. 4.

Among several impactor-target geometries used in the second plate-impact test series, we shall concern ourselves with only two types here. In the first geometry, the gage with its x-cut quartz buffer was placed on the back surface of the beryllium target and the transmitted compressive wave profile was measured (Fig. 3(b)). In the second geometry, the

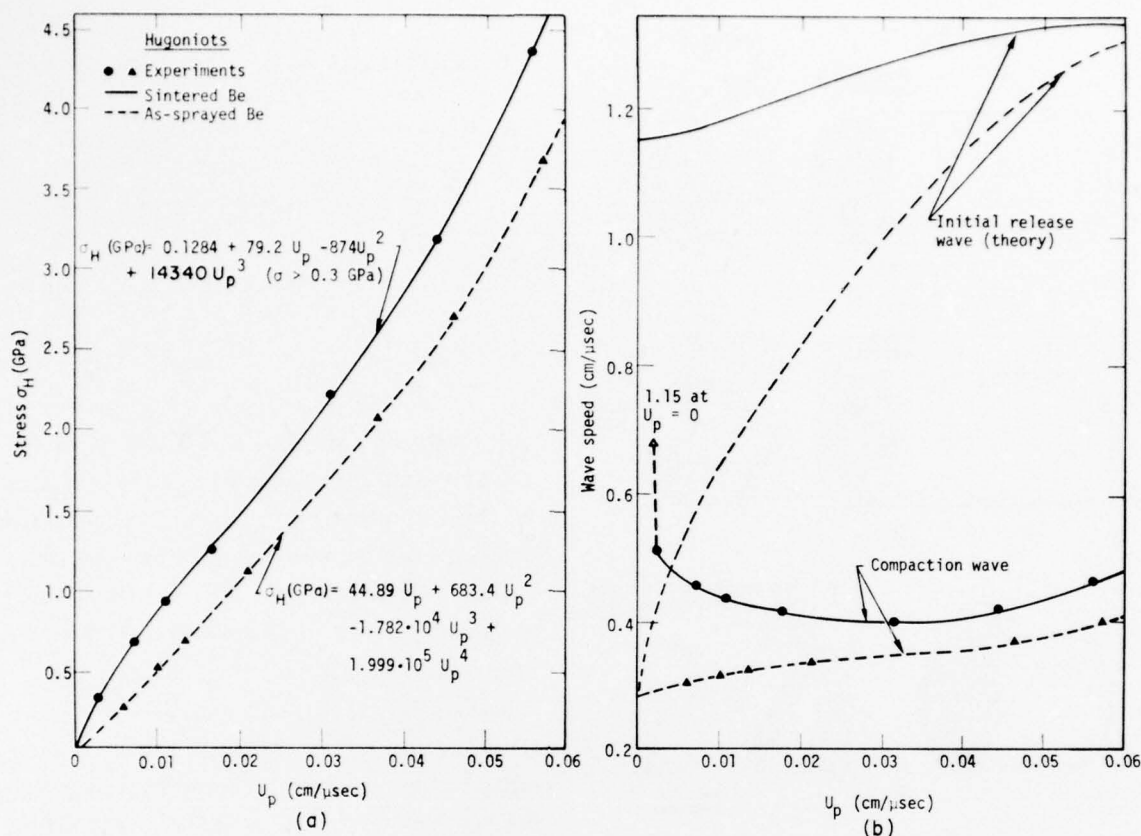


Fig. 4. (a) Hugoniot σ_H -vs- U_p points (solid dots and triangles) for porous beryllium and their analytical representations; (b) compaction speeds vs U_p obtained from Hugoniot relations, and initial release wave velocities calculated using Eqs. (4), (10), and bulk and shear moduli from ultrasonic measurements.

one used for most of the wave profiles reported here, carbon-Kapton* piezo-resistive "in-material" gages were positioned behind various thicknesses of specimen material (in effect, were at various depths in the material), as shown in Fig. 3(c). The gages, about 100 μ m thick, were located so that the wave disturbance at one gage could not reach

* DuPont trade name. Reference to a company or product name does not imply approval or recommendation of the product by the University of California or the U. S. Atomic Energy Commission to the exclusion of others that may be suitable.

other gages during the times of interest. This was accomplished by machining slots into the surfaces of each of the beryllium disks into which the gages were epoxied. Thus each gage at the rear of the stack received a wave transmitted only through a series of thin ($\leq 5 \mu$ m) epoxy glue lines. This procedure differs from other techniques where the surface is not slotted and gages at level 3, for instance, receive waves passing through nonnegligible discontinuities at levels 2 and 3. Computer calculations showed that the 5- μ m epoxy layers used to glue the gages onto the target plates were thin enough to ignore in future calculations.

The use of the in-material gages is advantageous, since they measure in situ stress profiles without the distortion caused by the major discontinuity presented by a "rear surface" gage or a free rear surface. Such techniques can reflect large compressive or release waves which affect the remainder of the wave in the sample. In-material gages, however, present their own class of problems, some of which are discussed in Ref. 18. Included (for the carbon gage) are nonlinear response, response time of approximately $0.1 \mu\text{s}$ which increases at stresses less than 0.5 GPa, and the likelihood of a previously unrecorded phenomenon of a change in piezoresistive coefficient when the gages are used in porous materials which subject the gage to microstretching. Application of in-material gages in porous samples is a relatively new concept. Those interested in further details should consult Refs. 3 and 18.

The gages measured wave profiles in the form of voltage-time oscillograms, which were later converted to stress-time histories using a voltage-stress calibration procedure. The accuracy of the wave profiles measured using in-material gages was affected by the following sources:

- (i) possible tilting of an impactor relative to the target at the time of impact,
- (ii) nonplanarity (hills and valleys) of the impact surface of the porous specimens, and
- (iii) local inhomogeneities through which the waves propagated.

Most of the wave arrival time errors originating from the tilt were corrected by using coaxial shorting pins to measure the degree of impactor tilt. The increase in apparent wave risetime from the tilt of the shock wave as it passed over the

sensitive element of the gage was not corrected for in the data analysis. In all but a few of the shots, however, the additional risetime was less than 20 ns and can be ignored.

The second difficulty was partly removed by applying a thin coat ($< 2 \mu\text{m}$) of impedance-matching epoxy to the impact surface to make a flatter and smoother surface. Nevertheless, the velocities calculated from the first signal arrival times measured at different gage stations were slightly irregular. To make a meaningful comparison between the experiments and the theoretical calculations, the experimental wave profiles were adjusted to conform to an average velocity. For the sintered materials, the experimental arrival times of the precursor were readjusted by fixing $0.62 \text{ cm}/\mu\text{s}$ as the velocity at 0.2 GPa for all measured wave profiles except for the two thickest specimens where the waves were attenuated below 0.2 GPa (in which case the arrival times were obtained using $1.15 \text{ cm}/\mu\text{s}$, the ultrasonic velocity, as the velocity at the foot of the wave fronts). The value of $0.62 \text{ cm}/\mu\text{s}$ was chosen by observing that the precursor front maintained a reasonably constant spreading as the precursor traversed the material. The "toe" of the precursor was assumed to travel at longitudinal sound speed, $1.15 \text{ cm}/\mu\text{s}$. Since the toe was not easy to observe on all wave profiles, the stress assumed to have a constant velocity was 0.2 GPa, slightly below the Hugoniot elastic limit of the material. Other stresses and their corresponding velocities were tested and gave approximately the same arrival times for the wave profiles.

For the as-sprayed materials, where no well-defined elastic wave was detected, a similar procedure gave less satisfactory results. In this case, we calculated U_s from the Hugoniot relations and Eq. (1b). It was in turn used as the compaction wave velocity at the midpoint of the peak stress level in the measured wave profiles. In general, the readjustment to the constant-

velocity criterion resulted in time shifts of less than $0.09 \mu s$, except for the thickest (1.9-cm) specimens, for which the time shifts were considerably larger. We noted, however, that the wave profiles at this thickness indicated rarefactions from the specimen edges had affected the wave forms to an extent that made the time adjustment of questionable value.

3. Description of the Porous Constitutive Model

Our model is based on Holt et al.'s P - α - τ model which is in turn a rate-dependent modification of Herrmann's model. The new features in our model are: (i) inclusion of deviatoric stresses, (ii) allowance for partial reopening of the pores upon unloading, (iii) use of an improved expression for the static compaction function, and (iv) use of a porosity-dependent relaxation time for pore closure.

3.1 FIRST CONSTITUTIVE RELATION: EOS OF POROUS MATERIALS

Two relations are used in the formulation of the constitutive model. The first relation is an equation which relates the pressure (P), volume (V), and energy (E) of a porous material to the equation of state (EOS) of the corresponding fully compacted solid (hereafter denoted simply as "solid" for brevity). The porosity parameter α is defined by this relation:

$$P(V, E) = \frac{1}{\alpha} P_s(V/\alpha, E_s), \quad E = E_s, \quad (2a)$$

which can be rewritten in an alternate but equivalent form,

$$\alpha = V/V_s = P_s/P, \quad E = E_s, \quad (2b)$$

where the subscript s refers to the solid material.

The first equality in Eq. (2b) states that the porosity parameter α is the ratio of the porous volume to the solid volume. The second equality in Eq. (2b) states that in taking the volume ratio the porous volume should be calculated at the porous pressure P which is smaller than P_s by a factor $1/\alpha$.¹⁹ (See points C' and C'' in

Fig. 5(a).) This is a physically reasonable procedure, since the pressure is the force per unit cross-sectional area, and since the cross-sectional area for the porous material is larger by a factor α .

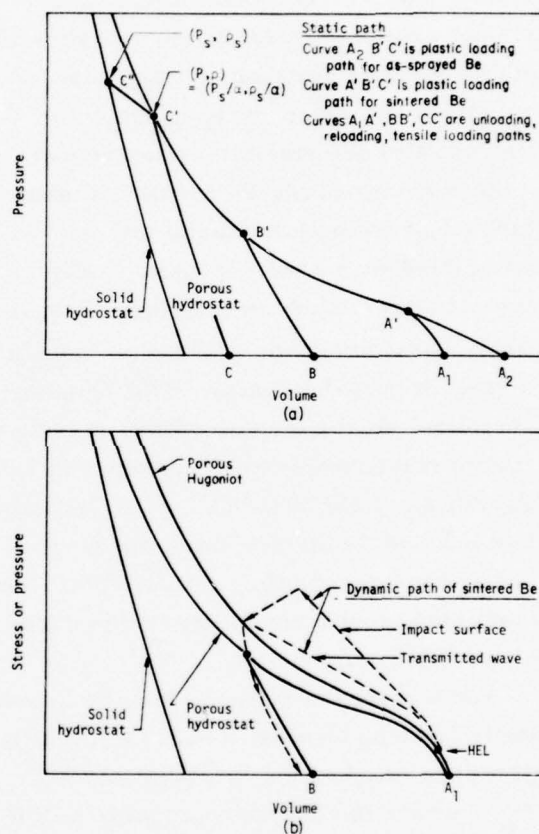


Fig. 5. (a) Schematic diagram showing porous and solid hydrostats. Loading and unloading paths for a porous material are also indicated. (b) Dynamic paths of a sintered porous sample are schematically shown. Note that these paths are not unique, and that wave profiles measured at points close to the impactor-target interface should contain more pronounced time-dependent effects than those obtained from a transmitted wave experiment.

3.2 SECOND CONSTITUTIVE RELATION: EQUATION FOR THE POROSITY PARAMETER

The second relation is an equation which describes a path for α during a time-dependent deformation process. Using the porous beryllium hydrostats in Fig. 2 as a guide, one can distinguish essentially two different types of paths that α must follow, namely plastic and elastic paths. The terms plastic and elastic used here refer to the irreversible and reversible portions of the pressure-volume paths under hydrodynamic (or hydrostatic) deformation. The irreversible behavior of the P-V path is characteristic of a porous material and is associated with a microscopic plastic flow of material adjacent to the pores, where local stress concentration is very large. It must be distinguished from an additional elastic-plastic effect, arising from a macroscopic shear stress and subsequent yield behavior, which is taken into account as the deviatoric stresses and is considered later. Figure 5(a) illustrates the elastic and plastic paths under hydrostatic deformation.

For sintered beryllium, loading follows initially along an elastic path ($A_1 A'$) until pressure reaches the "yield pressure" $P_{A'}$, where the microscopic plastic flow process begins to dominate over the local elastic strain contribution to P. We assume that this path is reversible upon unloading and is characterized by a relatively small compressibility on account of a large number of more spherical (hence stronger) pores present in the sintered specimen. Beyond point A', the deformation follows a plastic path ($A' B' C'$), which is mostly irreversible. Along this por-

tion of the P-V path the specimen is more easily compressed. The implication of a negative curvature at point A' for wave profile measurements is that such curvature introduces a precursor wave which precedes the main shock wave associated with the plastic path. In accordance with the static experiments, unloading from and reloading back to the plastic path ($A_1 \leftrightarrow A'$, $B \leftrightarrow B'$, and $C \leftrightarrow C'$ in Fig. 5(a)), as well as tensile loading ($P < 0$), are assumed to follow elastic paths.

For as-sprayed porous beryllium, the irregularly shaped pores and cracks present are more easily deformed (thus more easily closed) than the more spherically shaped pores in the sintered material (with which elastic deformation is associated). Therefore, plastic loading in the as-sprayed beryllium is assumed to start essentially at zero pressure, i.e., from point A_2 in Fig. 5(a). Such a P-V path will produce a wave profile without a precursor. Aside from this difference, deformation characteristics of the as-sprayed specimen are taken to be qualitatively similar to those of the sintered specimen, although the parameters in the model are quite different from each other.

3.2.1 Plastic Path

During dynamic loading processes such as those shown in Fig. 5(b), where the pressure and volume of porous materials lie above the static compaction path in Fig. 5(a) (curves $A_2 A' B' C'$ and $A' B' C'$ for as-sprayed and sintered beryllium, respectively), and α is still decreasing with time, we assume the porous materials follow a plastic path. Along this path we

use the rate-dependent pore-closure relation of Holt et al.,⁸

$$\alpha = g(P) - \tau d\alpha/dt, \quad (3)$$

The parameter τ is a time constant describing the rate of plastic flow of material into pores, which reduces α to a final average equilibrium value given by the static compaction function $g(P)$.

To determine $g(P)$, we eliminate V in Eq. (2) by using hydrostatic P-V data for porous specimens and similar P-V data for solid beryllium.¹⁷ The resulting data, P and $g(P)$, can be accurately represented by the following expression:

$$g(P) = \alpha_{\infty} + (\alpha_0 - \alpha_{\infty}) \exp(aP + bP^2 + cP^3), \quad (4)$$

where α_0 is the initial porosity and α_{∞} is introduced to account for some residual porosity that appears to persist under extremely high pressures.^{7,18} The constants a , b , and c are obtained by fitting the data by a least-squares method. Other mathematical representations used earlier,^{8,9} namely polynomials in P , did not represent the experimental data as well as Eq. (4) does. It is perhaps important to note that Eq. (4) is derived from the hydrostatic data; yet, as we shall see later, it plays a major role in reproducing dynamic data such as wave profiles.

There is a close similarity between Eq. (3) and another rate-dependent relation derived from a spherical model calculation for an elastic-viscoplastic material by Holt et al.¹³; i.e.,

$$P = P_{\text{static}}(\alpha) - \tau' d\alpha/dt, \quad \tau' \equiv 4\eta/[3\alpha(\alpha - 1)]. \quad (5)$$

In deriving Eq. (5), the inertial term,

which is small¹ compared to the viscous contribution $\tau' d\alpha/dt$, was neglected.

Equation (5) describes an approach of the dynamic pressure $P(\alpha, t)$ to the static value $P_{\text{static}}(\alpha)$, where α is an independent variable, while Eq. (3) describes an approach of the dynamic $\alpha(P, t)$ to the static value $g(P)$, using P as an independent variable. Since the two expressions represent the same relaxation process, the time constants τ and τ' will likely be equal or differ at most by a multiplicative constant. Assuming that this is true, and replacing the viscosity η in Eq. (5) in terms of α_0 and $\tau_0 (\equiv \tau \text{ at } \alpha_0)$, we obtain the following α -dependent τ :

$$\tau = \tau_0 \alpha_0 (\alpha_0 - \alpha_{\infty}) / [\alpha(\alpha - \alpha_{\infty})]. \quad (6)$$

Again, α_{∞} is used in place of unity to account for the observed behavior of α at high pressures.

Equation (6) gives a value for τ which is equal to τ_0 at the foot ($P = 0$) of the compressive wave front, but which becomes larger at higher stress levels. By choosing τ_0 small enough we can obtain calculated wave profiles for as-sprayed beryllium similar to those observed in plate impact tests, namely a steeply increasing portion at the foot which may become ramped (depending on P) at the peak stress level. It should be noted that, for physically reasonable systems, although τ becomes large at high pressures, $\tau d\alpha/dt$ in Eq. (3) always approaches zero.

3.2.2 Elastic Path

If the conditions for the plastic loading path are not satisfied, the porous material is assumed to follow an elastic path, where the pores respond instantaneously without

any time delay. Assumption of the time-independent elastic path has been checked to be nearly correct in the case of a hollow sphere in an aluminum matrix.²⁰

To obtain an equation for α along an elastic path, we first express the porous and solid EOS's in incremental form. That is, using Δ to denote the difference in P (and in P_s) at two successive time steps (differencing as used in a numerical hydrodynamic code), we have

$$\Delta P = K(\Delta \rho / \rho), \quad (7a)$$

$$\Delta P_s = K_s(\Delta \rho_s / \rho_s), \quad (7b)$$

where K and K_s are the bulk moduli of the porous and solid materials, respectively. The density ρ in Eq. (7a) is eliminated by using Eqs. (2a) and (7b).

After lengthy algebraic manipulation, we obtain an expression for the rate of change of α with P along the elastic path; i.e.,

$$d\alpha/dP = \alpha(K_s/K - \alpha)/(\alpha P - K_s). \quad (8)$$

In a numerical hydrodynamic code, the use of an incremental expression such as Eq. (8) rather than a specific form for α is preferred. That is, during the initial compaction, α switches from the elastic α_e given by a numerical integration of Eq. (8) to the plastic α_p given by solving Eq. (3) whenever α_e exceeds α_p . No additional parameter, such as the pressure at the elastic limit (point A' in Fig. 5(a)), is needed. Also, since Eq. (8) does not require K and K_s to be linearly elastic, any desired forms for K and K_s can be inserted whenever necessary.

Next, the bulk modulus K required in Eq. (8) and the shear modulus G required in the deviatoric stress must be specified.

For this purpose, Mackenzie's expressions¹⁰ for K and G , namely

$$1/K = \alpha/K_s + \frac{3(\alpha - 1)}{4G_s} + O[(\alpha - 1)^3], \quad (9a)$$

$$G = G_s - \frac{5G_s(K_s + 4G_s)}{9K_s + 8G_s} \frac{\alpha - 1}{\alpha} + O[(\alpha - 1)^2], \quad (9b)$$

for a linear elastic medium containing noninteracting spherical pores are rewritten; i.e.,

$$1/K = (\alpha_\infty/K_s)t + (1/K_0)(1 - t), \quad (10a)$$

$$G = (1/G_s)t + (1/G_0)(1 - t), \quad (10b)$$

$$t \equiv (\alpha_0 - \alpha)/(\alpha_0 - \alpha_\infty),$$

where the subscript 0 refers to the initial porous state. These expressions, which were first introduced by Seaman¹¹ (with $\alpha_\infty = 1$), are obtained directly by eliminating G_s in Eq. (9a) in terms of K_0 and α_0 , and K_s in Eq. (9b) in terms of G_0 and α_0 . The factor $(1 - t)$ in Eq. (10b) is actually $(1 - t)\alpha_0/\alpha$ which is approximated to $(1 - t) + O[(\alpha - 1)^2]$.

The use of Eq. (10) rather than Mackenzie's original expressions (Eq. (9)) is clearly preferred, since Eq. (10) is designed to reproduce the correct moduli at two limiting values of α , namely α_0 and α_∞ . The straightforward use of Mackenzie's expressions, Eq. (9), which are correct to $O[(\alpha - 1)^2]$ for K and $O(\alpha - 1)$ for G , will yield poor results for a material with a large porosity as well as for materials such as as-sprayed beryllium whose initial moduli K_0 and G_0 are greatly different from K_s and G_s , respectively.

3.3 YIELD STRESS

To complete the formulation the deviatoric stress s must be specified. Then, the axial stress σ_1 (along direction 1) in a 1-D strain deformation is given by

$$\sigma_1 = -P + s_1, \quad (11)$$

where

$$s_1 = \frac{4}{3} G \ln(V/V_0), \text{ if } |s_1| < \frac{2}{3} Y, \quad (12a)$$

$$= \pm \frac{2}{3} Y \text{ otherwise (+ for loading and} \\ \text{- for unloading).} \quad (12b)$$

The shear modulus G in Eq. (12a) is calculated from Eq. (10b). Y may be calculated from $\frac{2}{3} Y = \sigma_1 + P$ if experimental data are available for P and σ_1 . The data can be fitted by a functional form such as

$$Y = \text{Max} [Y_0, Y_1 + Y_2 \epsilon + Y_3 \epsilon^2], \quad (13)$$

where $\epsilon = \ln(V/V_0)$ and small elastic strain is neglected. We use $\ln(V/V_0)$ for ϵ rather than the equivalent plastic strain invariant ϵ_p , which is usually used in calculation of Y for solid materials. In most elastic-plastic theories of solids, ϵ_p is assumed to be a nondecreasing function of the strain history, and the resulting Y becomes also a nondecreasing function of ϵ_p , which is contrary to the cyclic loading and unloading data of Schock et al.⁵ mentioned in Sec. 2.2.

Apart from the parameter τ_0 , the formulation discussed above requires only static compression data and ultrasonic data at $P = 0$ to be measured in the porous material, and all other parameters can be determined from the properties of

the solid materials. In practice, such a procedure has not been successfully applied beyond 1 GPa, mainly because the 1-D strain experiment from which σ_1 is obtained requires a sophisticated technique of applying both confining stress and axial stress and is difficult to perform at higher stresses. Therefore, at pressures greater than the experimental limit of our static 1-D strain apparatus (~ 1 GPa) the Hugoniot stress (σ_H) rather than σ_1 was used to calculate Y . In the case of as-sprayed beryllium the data on σ_1 and σ_H agree nearly perfectly to 1 GPa, thus providing an experimental support for using σ_H in place of σ_1 at higher stresses. We note that the yield strength obtained in this manner exceeds the value (~ 0.2 GPa) corresponding to solid beryllium at some partially compacted volumes. Such a phenomenon would seem to be entirely possible, since the yield stress can increase through both the work hardening of the matrix material and the densification during deformation. At some region of partial compaction, therefore, the latter could give a dominant contribution to Y as would seem to be the case here.

The corresponding comparison for sintered beryllium gives an apparently inconsistent result. The comparison shows that σ_H lies above σ_1 , with the deviation becoming larger at higher strains. At $(V_0 - V)/V_0 = 0.04$, for example, σ_H is about 1.2 GPa while σ_1 is about 0.9 GPa. This disagreement is difficult to explain at present. The corrections to σ_1 or σ_H from the thermal contributions are too small to explain the differences. Also a possible rate-dependent correction to stress from viscous damping is a non-steady-state

process which would affect only the shape of the shock front, not the amplitude.²¹ The Hugoniot stresses were taken well behind the shock front and would, therefore, not be affected to a significant extent by the rate-dependent process. Further experimental and theoretical effort would seem to be useful to clarify this situation.

Having no clear preference of one choice of Y over another for sintered beryllium, we made two separate calculations on wave propagation to test the form of Y . For the first calculation, Y was taken to be constant (0.1 GPa). This choice was based on the assumption that overall differences in the hydrostat and σ_1 , which follow each other very closely to the highest stress level achieved in the static 1-D strain experiment (~ 1 GPa), can be approximately represented by using the constant yield strength (~ 0.1 GPa).

Actually the static data in the region of compaction near the yield point present a more complex picture than the constant Y assumption used here, since second order effects (e.g., material anisotropy) which are known to exist in porous beryllium but which were ignored in our analysis, become relatively more signifi-

cant here. Numerous attempts were made to reconcile the yield behaviors as measured in the different experiments. In the end, the pragmatic view was taken that the more sophisticated forms of the yield, when placed in the hydrocode, did not produce significant differences in the predicted wave profiles investigated here. At low stress levels (≤ 0.3 GPa), however, a refined model may be needed in the future to account for the anisotropic effect explicitly.

For the second calculation, Y was obtained from $1.5 (\sigma_H + P)$, i.e., Eqs. (11)-(12), using the data on σ_H and P . The resulting numerical values of Y were fitted by a polynomial form of Eq. (13).

A test calculation was carried out using shot geometry identical to shot BU-B (see Fig. 8(d) in the next section). The result showed that the constant Y method generally gave much better agreement with experiment than Y obtained from a fit to the σ_H - P data. In the latter case, the compressive wave front had a faster rise-time and was traveling so fast that the experimentally observed attenuation did not take place in the computer calculation. The calculations shown in Sec. 5 were made using $Y = 0.1$ GPa.

4. Computational Procedure

Solutions of Eqs. (2a) and (3) give α_p ($=\alpha$) applicable to the plastic path, while Eqs. (2a) and (8) give the elastic solutions α_e . Since both pairs of equations are highly complex, we solve them iteratively in the hydrodynamic code KO.¹⁵ Iterative schemes for both cases are similar, however, so a single scheme was adopted to take care of both cases.²²

We introduce a function $F_\alpha(P)$,

$$F_\alpha(P) = \begin{cases} \alpha_e, & \text{if } \alpha_e \leq \alpha_g, \text{ or } \alpha^N < \alpha_p, \\ & \text{or } P \leq 0, \quad (14a) \\ 1, & \text{if } \alpha_e \text{ or } \alpha_p < 1, \quad (14b) \\ \alpha_p, & \text{otherwise,} \quad (14c) \end{cases}$$

where the superscript N represents the present time step in a finite-difference scheme used in the code, and α_e , α_g , and α_p are defined by

$$\begin{aligned} \alpha_e &= \alpha^N + (P - P^N)(d\alpha/dP), \\ (d\alpha/dP) &= \text{Eq. (8) at } \alpha = \alpha^N, \quad (15a) \\ \alpha_g &= g(P^{N+1/2}), \quad P^{N+1/2} = (P + P^N)/2, \quad (15b) \\ \alpha_p &= (\alpha_g - \alpha^N/2 + \alpha^N \tau/\Delta t)/(0.5 + \tau/\Delta t). \end{aligned} \quad (15c)$$

That is, $F_\alpha(P)$ is set to α_e if (i) α_e lies below the static compaction path α_g , or (ii) the dynamic value α_p at the next time step starts to decrease, or (iii) the zone under consideration is in tension.

We also define the second function $F_P(\alpha)$, which is Eq. (2a) evaluated at the $(N+1)$ th time step, except that the correct α is yet to be determined; i.e.,

$$F_P(\alpha) = \frac{1}{\alpha} P_S (V^{N+1}/\alpha, E^{N+1}). \quad (16)$$

The basic idea behind the scheme is to enclose a desired solution by a two-dimensional "box" with its sidelengths $\alpha'' - \alpha' (>0)$ and $P'' - P' (>0)$, and to reduce the size of the box (holding the solution) in each iterative cycle until the solution has converged within a desired accuracy. Specifically, this is done as follows:

(1) Initial box size:

$$\begin{aligned} \alpha' &= \text{Min}[\alpha^N, F_\alpha(F_P(\alpha^N))], \\ \alpha'' &= \text{Max}[\alpha^N, F_\alpha(F_P(\alpha^N))], \\ P' &= \text{Min}[P^N, F_P(F_\alpha(P^N))], \\ P'' &= \text{Max}[P^N, F_P(F_\alpha(P^N))]. \end{aligned}$$

(2) Iterative loop:

$$\begin{aligned} \text{(i)} \quad \alpha_A &= (\alpha' + \alpha'')/2, \\ P_A &= (P' + P'')/2. \end{aligned}$$

(ii) α -iteration to obtain new α' and α'' :

$$\begin{aligned} \alpha_B &= \text{Min}[\alpha_A, F_\alpha(F_P(\alpha_A))], \\ \alpha_C &= \text{Max}[\alpha_A, F_\alpha(\alpha_A)], \\ \alpha' &= \text{Max}[\alpha', \alpha_B], \\ \alpha'' &= \text{Min}[\alpha'', \alpha_C]. \end{aligned}$$

(iii) P-iteration to obtain new P' and P'' :

$$\begin{aligned} P_B &= \text{Min}[P_A, F_P(F_\alpha(P_A))], \\ P_C &= \text{Max}[P_A, F_P(F_\alpha(P_A))], \\ P' &= \text{Max}[P', P_B], \\ P'' &= \text{Min}[P'', P_C]. \end{aligned}$$

(3) Convergence criterion:

The convergence test for $|P'|$ $\leq 10^{-7}$ GPa is

$$\left| \frac{\alpha' - \alpha''}{\alpha'} \right| + |P'| < 0.005;$$

the convergence test for $|P'| > 10^{-7}$ GPa is

$$\left| \frac{\alpha' - \alpha''}{\alpha'} \right| + \left| \frac{P'' - P'}{P'} \right| < 0.005.$$

If the inequality holds, we take $\alpha = (\alpha' + \alpha'')/2$ and $P = (P' + P'')/2$ as our final solutions; otherwise, the program returns to the next iterative loop.

Note that the above scheme performs essentially two separate iterations, one on α and another on P , rather than the usual way which relies on a single iteration loop on α , since P is the dependent variable of α . This precaution was necessary, for P can change enormously for a slight change in α , especially near the

region of complete compaction. (See Ref. 14 for further details.)

Summarized in Table 2 are the exact numerical values that were used in the wave-profile calculations for porous beryllium. A constant τ was used for sintered beryllium, since it gave a slightly better wave profile than the one obtained from Eq. (6). The difference is minor, however. The values of K_0 and G_0 are those obtained from ultrasonic measurements. The expressions for $g(P)$ and Y are applicable to pressures less than 4 GPa. Application of these formulae to higher stresses is subject to uncertain error.

Calculation of wave propagation also requires knowledge of accurate EOS data

Table 2. Numerical values used in the wave profile calculations for porous beryllium.

Static compaction function (Eq. (4))

$\alpha_\infty = 1.02$, $P < 4$ GPa.

Sintered Be: $a = 0.1212$ (GPa) $^{-1}$, $b = -0.7994$ (GPa) $^{-2}$, $c = 0.1361$ (GPa) $^{-3}$.

As-sprayed Be: $a = -0.4822$ (GPa) $^{-1}$, $b = -0.4355$ (GPa) $^{-2}$, $c = 0.6975$ (GPa) $^{-3}$.

Relaxation time for pore closure

Sintered Be: $\tau = 0.04$ μ s (constant τ).

As-sprayed Be: $\tau_0 = 0.006$ μ s (porosity-dependent τ from Eq. (6)).

Bulk and shear moduli (Eqs. (10a), (10b))

$K_s = 122$ GPa, $G_s = 155.6$ GPa.

Sintered Be: $K_0 = 74$ GPa, $G_0 = 108.9$ GPa.

As-sprayed Be: $K_0 = 19.4$ GPa, $G_0 = 0$.

Yield stress (Eq. (13))

Sintered Be: $Y = 0.1$ GPa.

As-sprayed Be: $Y = \text{Max} (0, -0.21 + 15.75\epsilon - 54\epsilon^2)$, $\epsilon < 0.146$,
 $= 0.146$, $\epsilon \geq 0.146$.

for the impactor, gage, buffer, and backing materials as well as the EOS of solid beryllium. Analytical expressions used to represent these materials are given in Table 3. The expressions for fused quartz and PMMA are obtained by fitting Barker and Hollenbach's data²³ with an additional small energy-dependent correction.^{24,25} The expression for x-cut quartz was obtained by fitting Graham's data.²⁶ The Grüneisen γ of x-cut quartz is small and is not well known. Therefore no energy-dependent correction was used for this material. The EOS of the carbon-Kapton

gage was generated by a least-squares fit routine to data on σ (GPa) vs U_P (cm/ μ s) ($\sigma = 0.22385 U_P + 0.0470 U_P^2$). The data was obtained in separate experiments conducted in a fused quartz target with carbon-Kapton in-material gages.¹⁸

Finally, we use the Grüneisen form of EOS for solid beryllium given in Ref. 27. This expression agrees closely with a similar expression in Ref. 17 for a small E . Since the energy-dependent correction is very small for plate impact tests, no apparent difference occurs in our calculation by using either this or the other expression.

Table 3. Expressions for the equations of state (EOS) of the carbon-Kapton gage, fused quartz, x-cut quartz, PMMA, and beryllium. P = pressure (GPa) and E = internal energy per original volume (GPa).

Material	EOS ($\mu \equiv \rho/\rho_{s0} - 1$)	ρ_{s0} (g/cm ³)
Carbon-Kapton	$P = 4.310 \mu + 1.904 \mu^2 + 294.3 \mu^3$	1.33
Fused quartz	$P = 77.56 \mu - 480.7 \mu^2 + 3074 \mu^3 + 7.52 E$	2.201
X-cut quartz	$P = 86.66 \mu + 45.87 \mu^2$	2.65
PMMA	$P = 10.09 \mu + 6.272 \mu^2 + 85 E$	1.184
Beryllium	$P = \frac{118.4 \mu (1 + 0.42 \mu - 0.08 \mu^2)}{(1 - 0.124 \mu)^2} + (116 + 16 \mu) E$	1.85

5. Comparison Between Predicted and Experimental Wave Profiles

Experimental wave profiles which will be used for comparison were obtained at two stress levels, approximately 0.6 and 1.7 GPa. Profiles were obtained by impacting a PMMA plate onto either sintered or as-sprayed porous beryllium having carbon-Kapton gages embedded at as many as six different depths within the material. Thus a single experiment took data on wave profiles at several different levels. The gages were located as deep as 1.9 cm from the impact surface and some measurement times extended up to 4 μ s. The resulting 21 wave profiles—both unattenuated and attenuated—represent large variations in the physical parameters and enabled us to extensively test the model. Experimental parameters (shot names, thicknesses of impactors, target specimens, and gages, measured peak stresses, durations of the measurements, etc.) are summarized in

Tables 4 and 5 for the sintered and as-sprayed porous specimens. In the computation the thicknesses of the backing materials (which were placed behind the gages to carry off the wave without reflection) are reduced from the original (experimental) thicknesses in some cases (Tables 4 and 5) since this saved the computing time without affecting the calculated stress histories.

Measured and computed wave profiles are compared in Figs. 6, 7, and 8 for the sintered material and in Figs. 9, 10, and 11 for the as-sprayed material. Note that abridged notations such as shot BT-A and shot BT-B are used here to indicate that the stress profiles were recorded at levels A and B in shot BT. Agreement between the experimental wave profiles and those predicted from the present model is good both quantitatively and

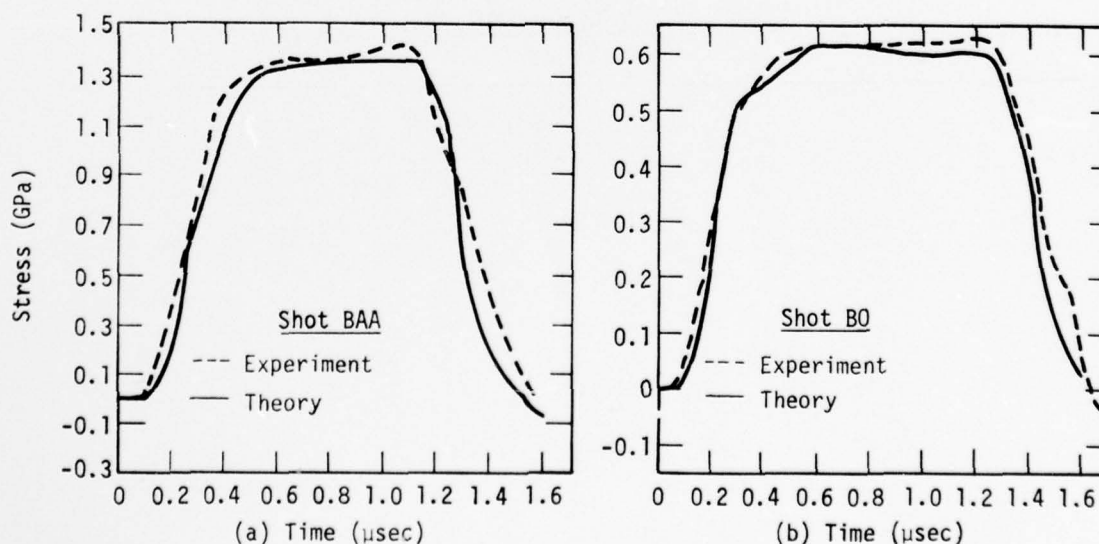


Fig. 6. Computed and measured full wave profiles for the sintered porous Be specimen at (a) high and (b) low stress levels. See Table 4 for experimental parameters used in these shots.

Table 4. Shot geometries used to measure the stress history of plasma-sprayed sintered porous beryllium ($\rho_0 = 1.660 \text{ g/cm}^3$).

Shot No.	Name	Impactor		Sintered Be		Target		Backing (sintered Be)		Maximum measuring time (μ s)
		Type ^a thickness (cm)	Velocity (cm/ μ s)	Thickness (cm)	Gage or buffer		Type ^a thickness (cm)	Peak stress (GPa)	Type ^a thickness (cm)	
					Type ^a thickness (cm)	Peak stress (GPa)				
1.	BAA	PMMA/0.1908	0.0561	0.1034	CK/0.0102	1.35-1.4	BES/0.8999	0.8999	1.6	
2.	BO	PMMA/0.1960	0.0237	0.1026	CK/0.0091	0.65	BES/0.7483	0.7487	1.6	
3.	BS-A	PMMA/0.1308	0.0556	0.4391	CK/0.0091	Atten. ^b	BES/1.4916	1.22	2.5	
4.	BS-B	PMMA/0.1308	0.0556	1.9358	CK/0.0091	Atten.	BES/0.4719	0.4	2.2	
5.	BU-A	PMMA/0.1245	0.0262	0.1280	CK/0.0119	0.66	BES/1.8029	0.65	1.1	
6.	BU-B	PMMA/0.1245	0.0262	0.3028	CK/0.0130	Atten.	BES/3.5387	1.12	2.2	
7.	BU-C	PMMA/0.1245	0.0262	0.4300	CK/0.0099	Atten.	BES/1.4857	1.223	2.5	
8.	BU-D	PMMA/0.1245	0.0262	1.9210	CK/0.0079	Atten.	BES/0.4719	0.4	2.2	
9.	BG-A	FQZ/0.9525	0.0259	0.1008	XQZ/0.3195	1.6-1.7	XQZ/0.6368	0.6368	1.5	
10.	BG-B	FQZ/0.9525	0.0259	0.7137	XQZ/0.3193	—	XQZ/0.6365	0.6365	2.3	
11.	BH-A	FQZ/0.9525	0.0306	0.1953	XQZ/0.3195	~1.8	XQZ/0.6398	0.6398	1.8	
12.	BH-B	FQZ/0.9525	0.0306	0.4183	XQZ/0.3196	—	XQZ/0.6373	0.6373	2.0	

^aFQZ = fused quartz, CK = carbon-Kapton gage, XQZ = x-cut quartz, BES = sintered porous beryllium.

^bAttenuated from the initial peak stress level of 1.4 GPa.

Table 5. Shot geometries used to measure the stress history of as-sprayed porous beryllium ($\rho_0 = 1.591 \text{ g/cm}^3$).

Shot No.	Name	Impactor (PMMA)		As-sprayed Be		Target		Backing (as-sprayed Be)		Maximum measuring time (μ s)
		Thickness (cm)	Velocity (cm/ μ s)	Thickness (cm)	Carbon-Kapton gage	Thickness (cm)	Peak stress (GPa)	Actual thickness (cm)	Thickness used in computation (cm)	
1.	BP	0.1905	0.0644	0.1027	0.0089	1.6	0.4717	0.35	1.7	
2.	BQ	0.1976	0.0237	0.1027	0.0093	0.53	0.4785	0.40	1.7	
3.	BT-A	0.1245	0.0750	0.	0.0114	1.7	1.5466	0.15	0.5	
4.	BT-B	0.1245	0.0750	0.1273	0.0124	1.7	1.4183	0.40	1.1	
5.	BT-C	0.1245	0.0750	0.3066	0.0112	Atten.	1.2441	0.40	2.5	
6.	BT-D	0.1245	0.0750	0.4313	0.0099	Atten.	1.121	0.40	2.8	
7.	BT-E	0.1245	0.0750	0.5497	0.0152	Atten.	0.9962	0.47	3.6	
8.	BT-F	0.1245	0.0750	0.6830	0.0127	Atten.	0.8689	0.65	4.1	
9.	BR-A	0.1245	0.0258	0.	0.0152	0.55	1.5466	0.20	0.67	
10.	BR-B	0.1245	0.0258	0.1288	0.0089	0.55	1.4310	0.25	1.2	
11.	BR-C	0.1245	0.0258	0.3038	0.0112	Atten.	1.2563	0.45	2.5	
12.	BR-D	0.1245	0.0258	0.4346	0.0114	Atten.	1.1222	0.45	2.8	
13.	BR-E	0.1245	0.0258	0.6980	0.0127	Atten.	0.8600	0.45	3.6	

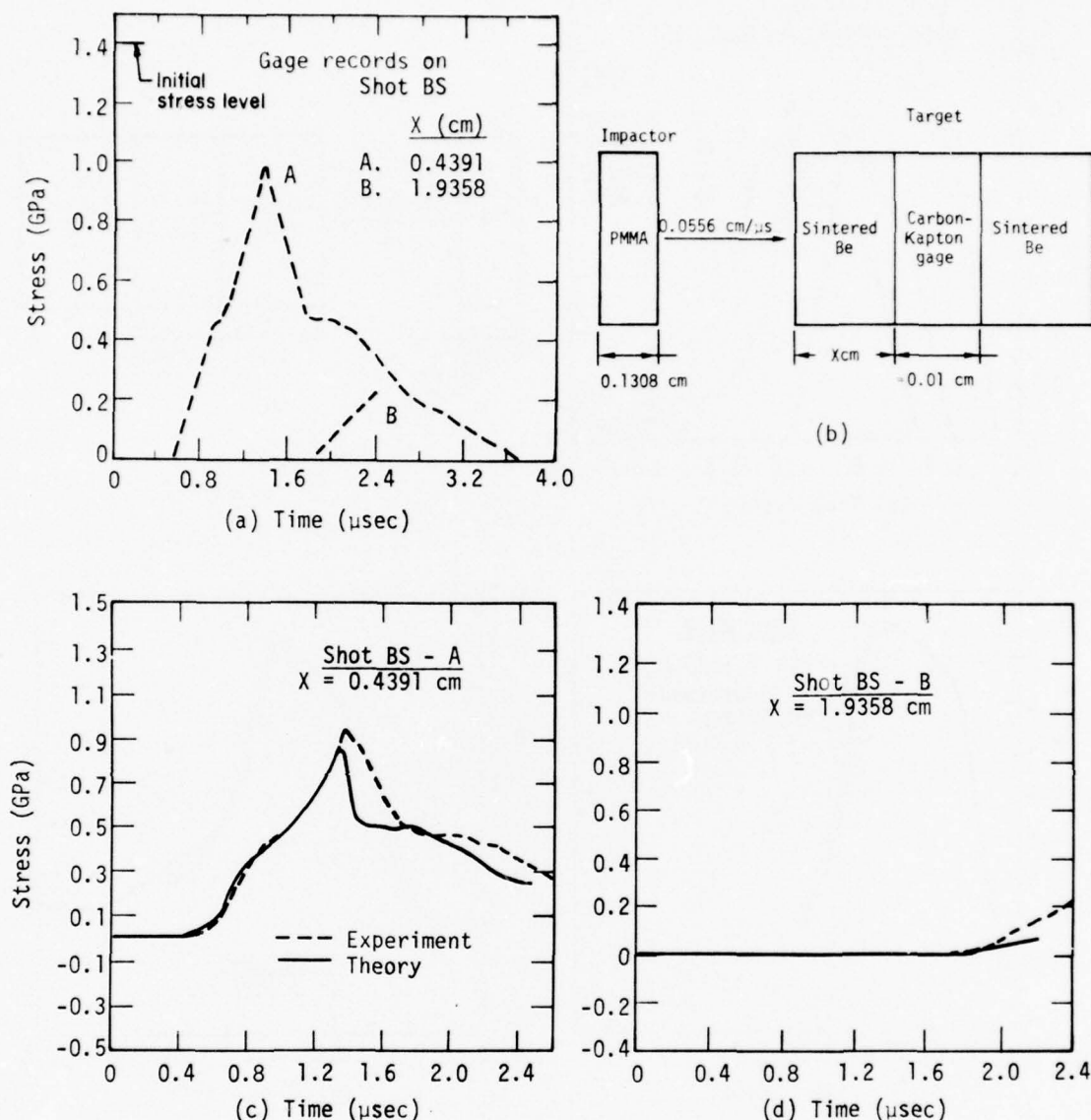


Fig. 7. Attenuated wave profiles of the high-stress shot (shot BS) for sintered porous Be: (a) experimental gage records, (b) impactor-target geometry (see also Table 4), (c)-(d) comparison of measured and computed wave profiles at different target thicknesses. (See text for possible corrections to shot BS-B.)

qualitatively. We give below more detailed comparisons of the compressive and release portions of these wave profiles and discuss several interesting features, including the effect of gage interaction on the wave profiles.

5.1 COMPRESSIONAL WAVES

For sintered porous beryllium (Figs. 7 and 8), an elastic precursor about 0.4 GPa high, which corresponds to the "shoulder" in the hydrostat in Fig. 2, precedes the

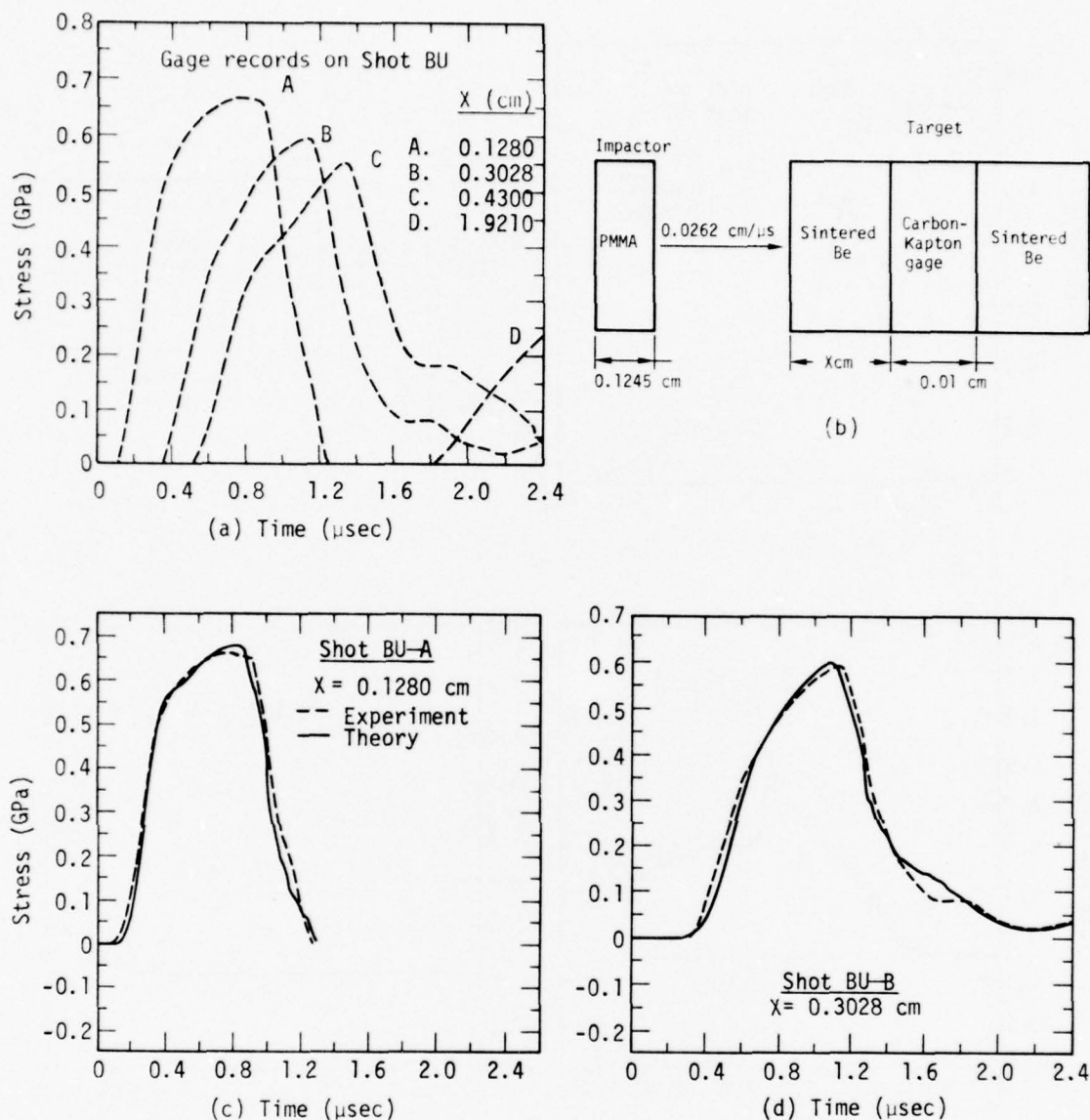


Fig. 8. Full and attenuated wave profiles of the low-stress shot (shot BU) for sintered porous Be: (a) experimental gage records, (b) impactor-target geometry (see also Table 4), (c)-(f) comparison of measured and computed wave profiles at different target thicknesses. (See text for possible corrections to shot BU-D.)

main plastic wave. At the foot of the precursor the velocity is close to the longitudinal sound speed, but it becomes slower at higher stresses. The value 0.62 cm/ μ s at $P = 0.2$ GPa chosen for the calculation of the first arrival times agrees reason-

ably well with the velocity of the precursor at this level.

Figures 12 and 13 give comparisons of the development of the non-steady-state shock wave and the precursor. These transmitted compressive profiles were

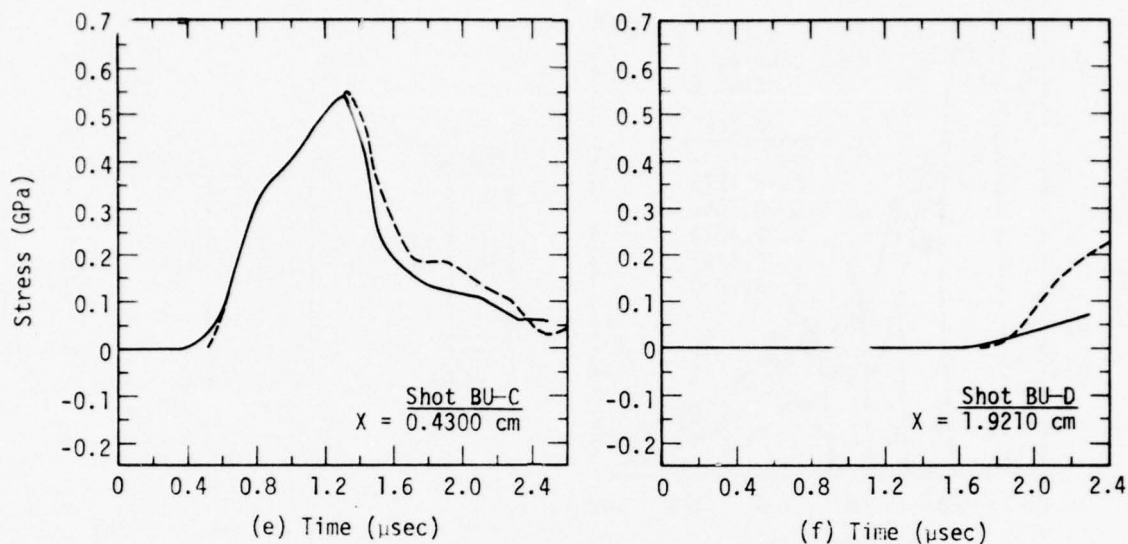


Fig. 8. (Continued)

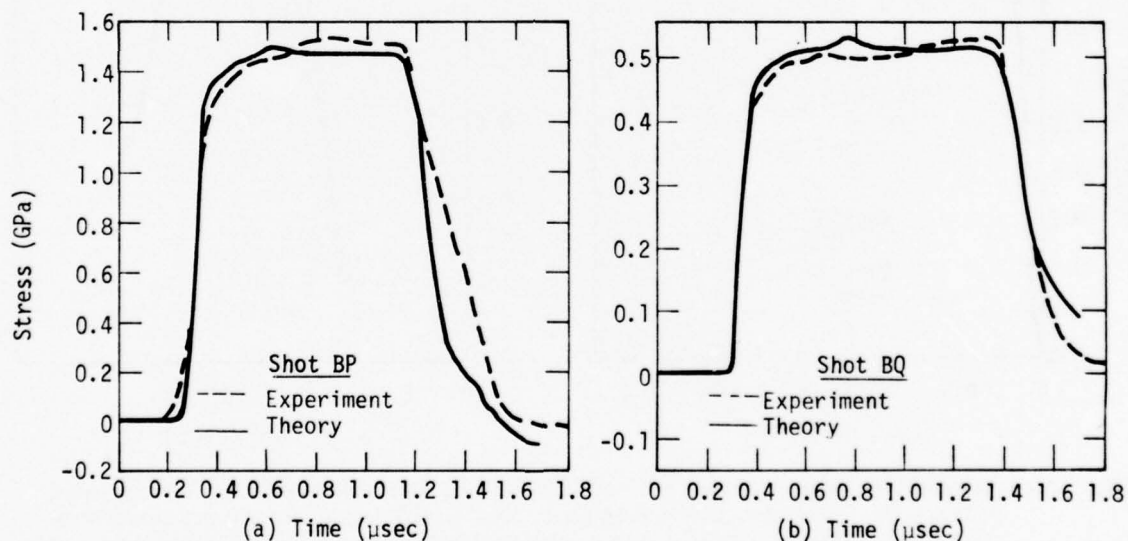


Fig. 9. Computed and measured full wave profiles for as-sprayed porous Be at (a) high and (b) low stress levels. See Table 5 for experimental parameters used in these shots.

measured at four different thicknesses by x-cut quartz gages. The impactor-target arrangement of Fig. 3(b) was used here. We note that agreement between the predicted and experimental wave profiles is satisfactory.

A faster-rising shock front and the lack of an elastic precursor are two chief distinguishing features of compressive profiles in as-sprayed porous beryllium.

Good agreement along the compressive portion of the wave has largely resulted

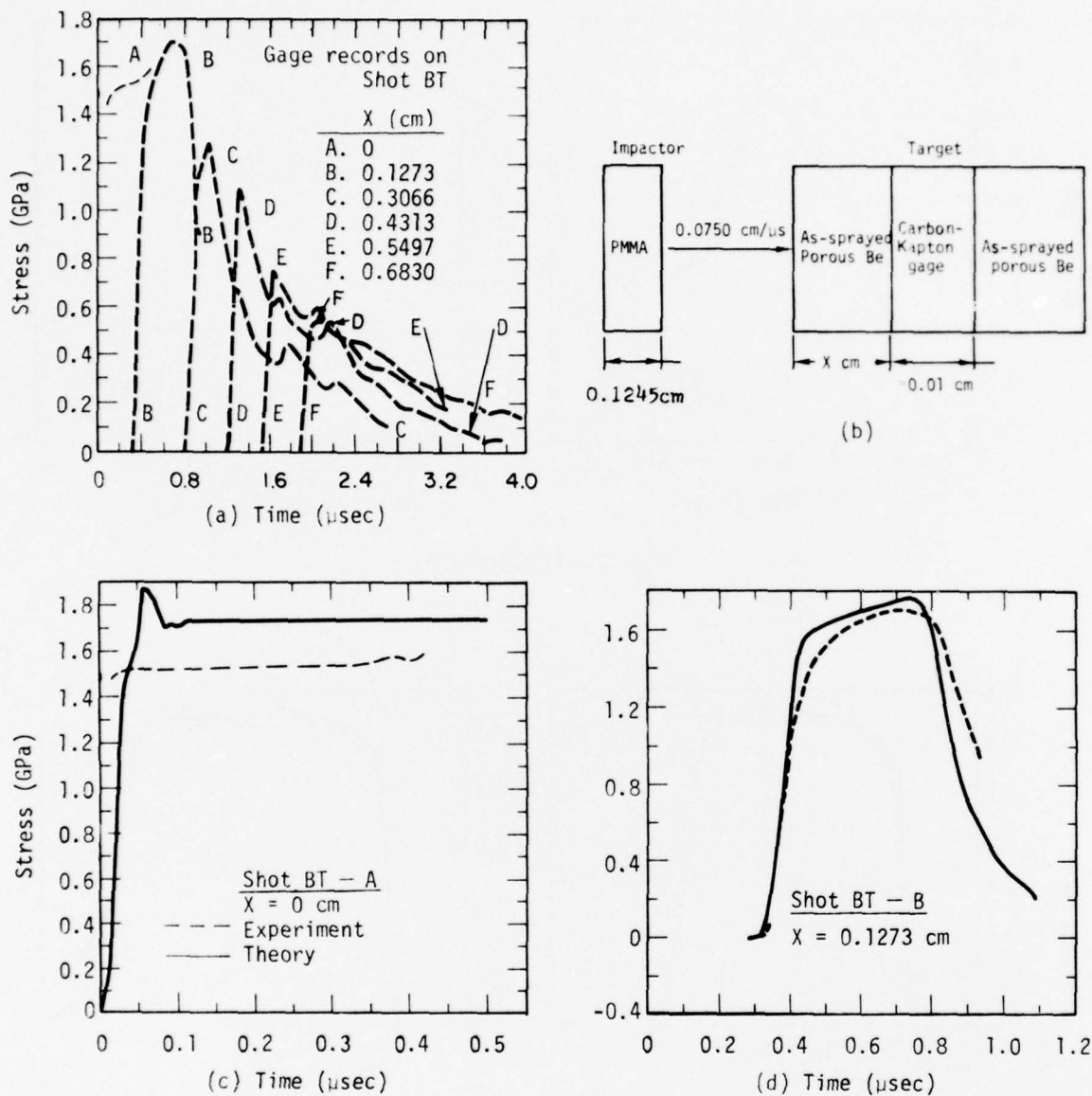


Fig. 10. Attenuated wave profiles of the high-stress shot (shot BT) for as-sprayed porous Be: (a) experimental gage records, (b) impactor-target geometry (see also Table 5), (c)-(h) comparison of measured and computed wave profiles at different target thicknesses. (See text for possible corrections to shots BT-A and BT-B.)

from the use of a new static compaction function having an exponential form rather than earlier expressions^{8,9,11} which use polynomials of $(P_c - P)/(P_c - P_e)$ or $(\rho_c - \rho)/(\rho_c - \rho_e)$. (The subscript c indi-

cates full compaction, and e indicates elastic limit, i.e., point A' in Fig. 5(a).) For materials which stay porous over a relatively large range of pressure, a single polynomial expression (even as

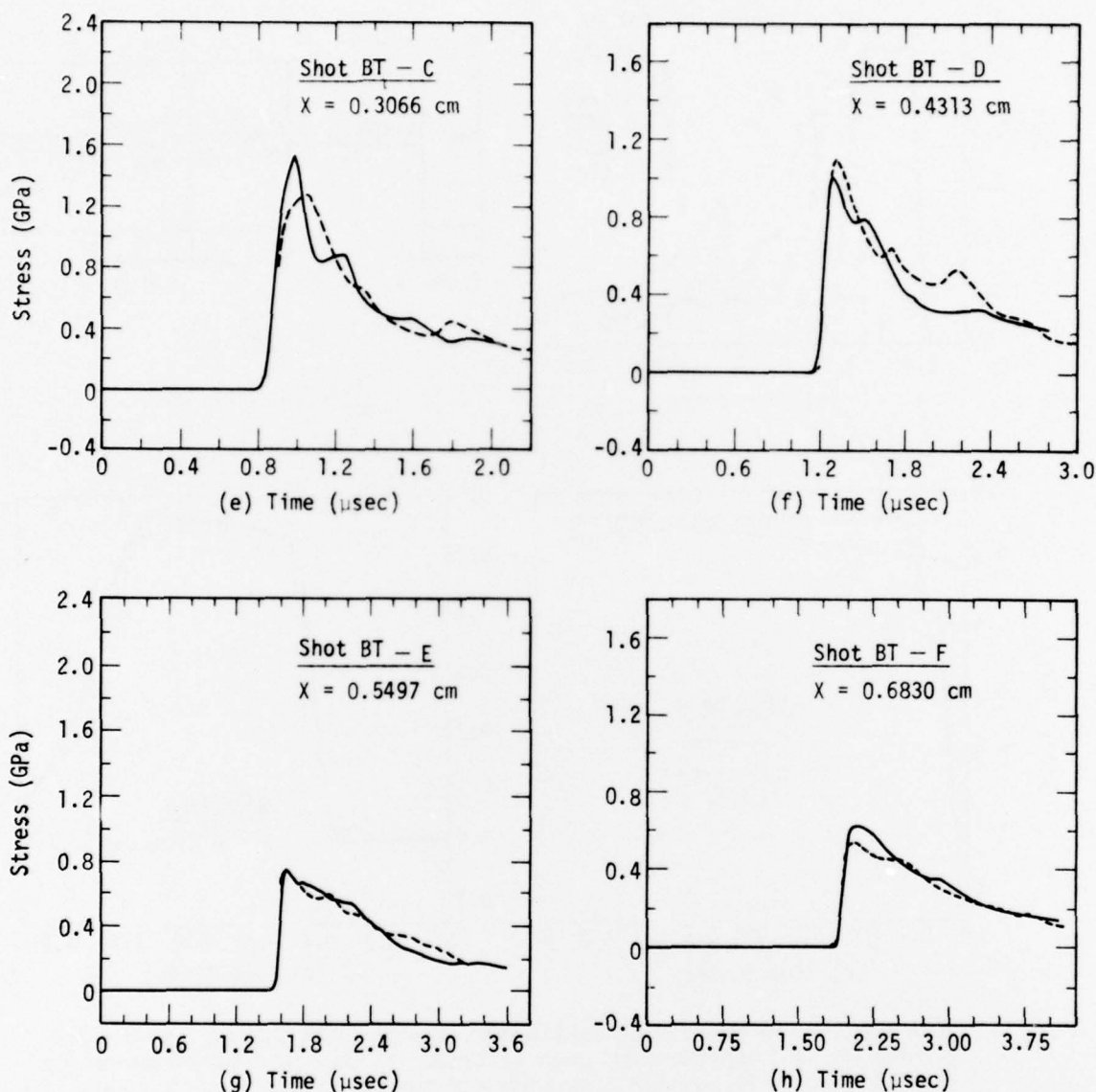


Fig. 10. (Continued)

high as fifth-order) is not adequate to represent the static compaction curve over the pressure range of interest.

We also note from Figs. 6-11 that the arrival times of the shocks (and their precursors in the case of sintered specimens) agree satisfactorily. The relaxation time $\tau = 0.04 \mu\text{s}$ matches the observed risetimes of the shocks in the case of the sintered specimens, while the porosity-

dependent τ from Eq. (6) adequately describes the risetimes of the shocks in the as-sprayed specimens. In the latter case, it is noteworthy that τ changes from $0.060 \mu\text{s}$ at the foot of the shocks to $0.015 \mu\text{s}$ at 1.7 GPa. If, instead of Eq. (6), a constant value ($0.015 \mu\text{s}$) had been used for τ , the foot of the shocks would be traveling too fast, resulting in much longer risetimes than those in the observed profiles.

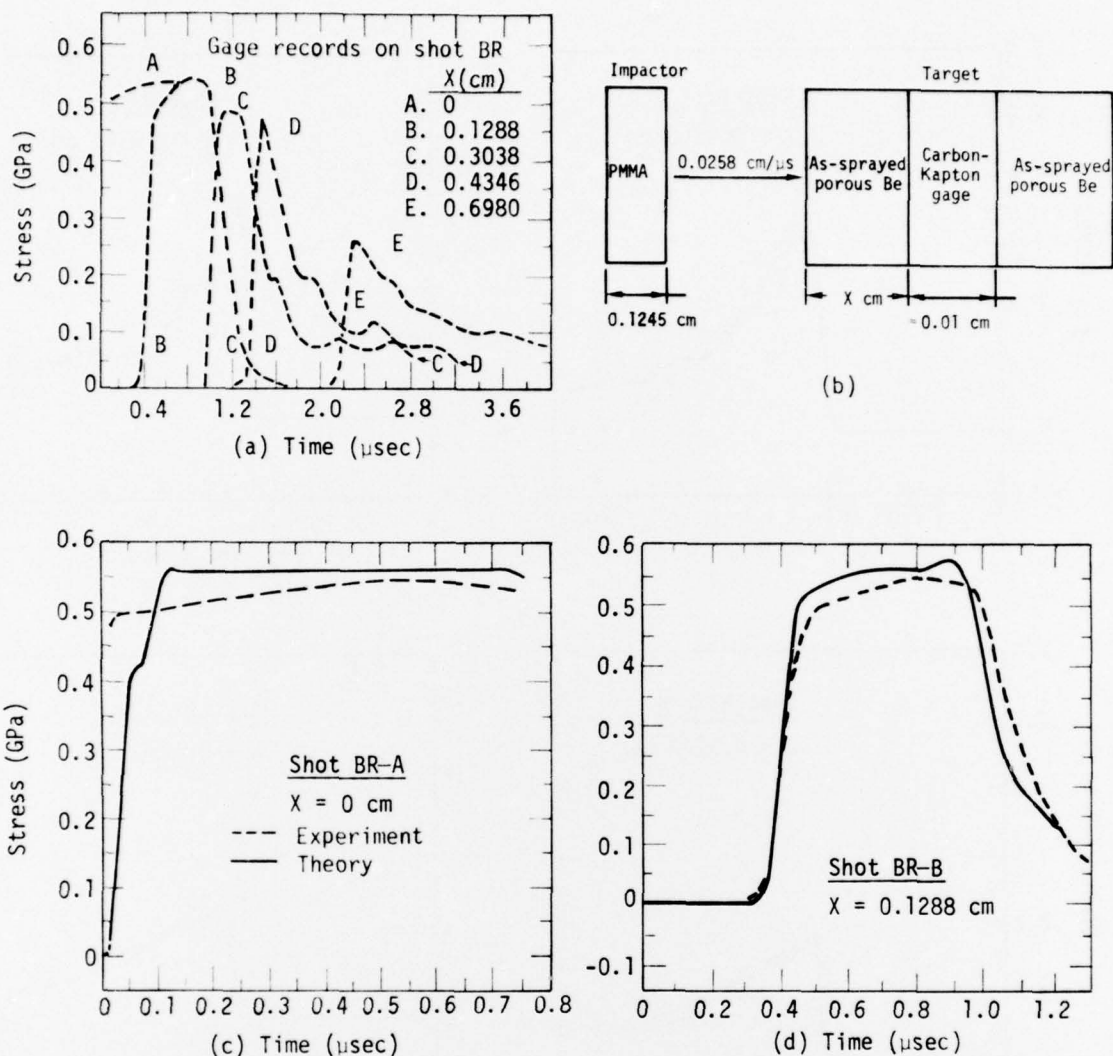


Fig. 11. Attenuated wave profiles of the low-stress shot (shot BR) for as-sprayed porous Be: (a) experimental gage records, (b) impactor-target geometry (see also Table 5), (c)-(g) comparison of measured and computed wave profiles. (See text for possible corrections to shots BR-A and BR-C.)

The largest deviation occurs in the calculation of the peak stresses, with the experimental data lying about 10% or less below computer predictions (except for shot BT-A in Fig. 10 and shots BR-A and BR-C in Fig. 11). Either experimental uncertainties or approximations in the model or a combination of the two could account for these relatively small differences. Experimental profiles of shots

BT-A and BR-A are anomalous in that the peak stresses recorded in the gages lie below the peak stresses recorded deeper within the material. (Compare the peak stress levels between shots BT-A and BT-B in Fig. 10 or shots BR-T and BR-B in Fig. 11.) Microstretching of the gages or macrostretching of the gage leads may account for an apparent lower stress at this surface.

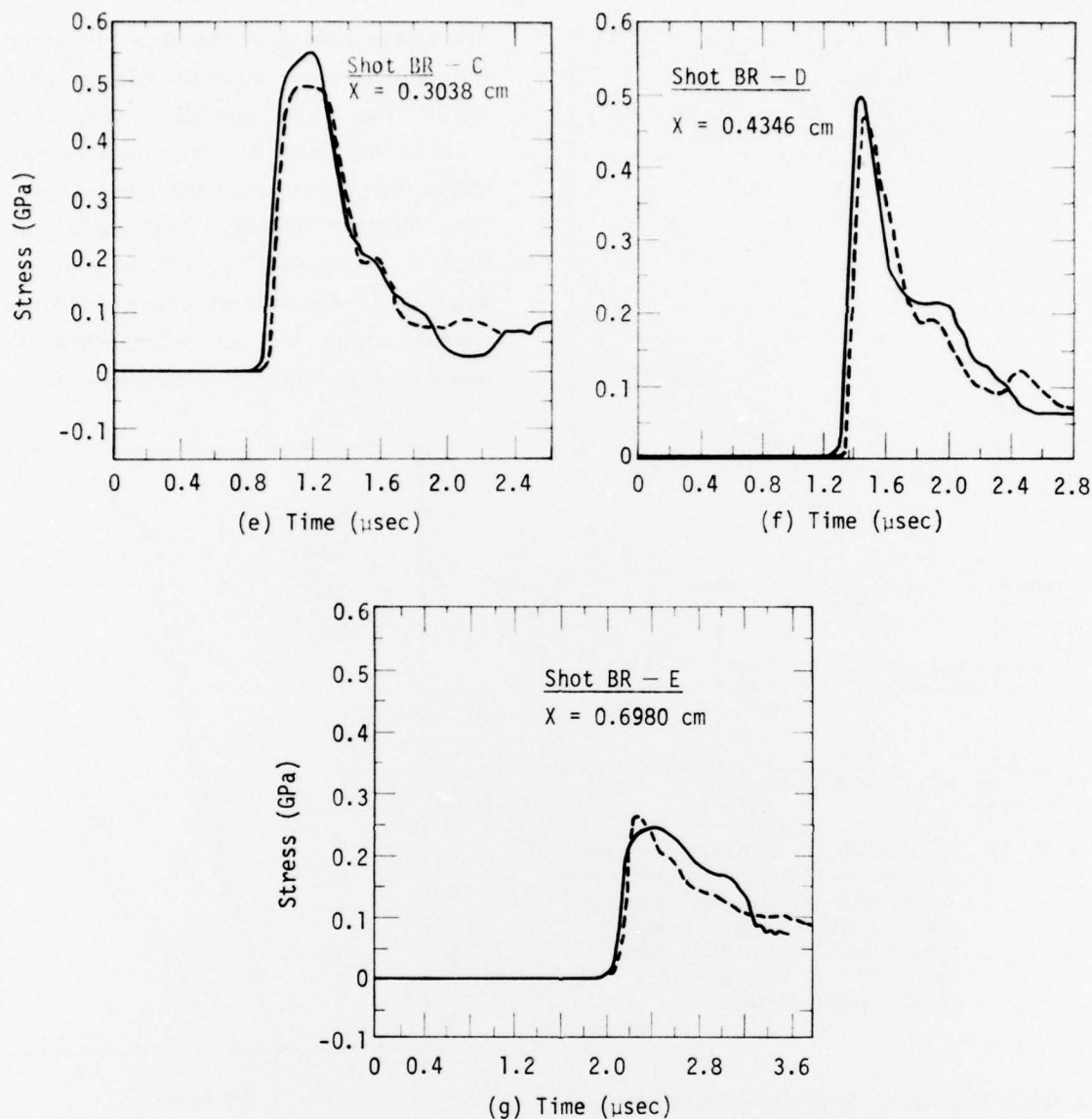


Fig. 11. (Continued)

5.2 GAGE EFFECT

It is difficult to carry out a meaningful analysis of wave profiles without considering the presence of the in-material (carbon-Kapton) gage. Although the gage itself is very thin ($\leq 0.01 \text{ cm}$), the discontinuity at

the plane of the gage alters the wave profiles in several important ways.

First, when a relatively sharp compression front encounters the gage (such as observed in shots BT-A, BR-A, and BR-C), the gage response is not instantaneous, but because the wave has to travel through

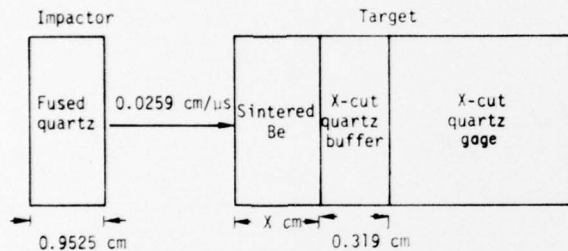
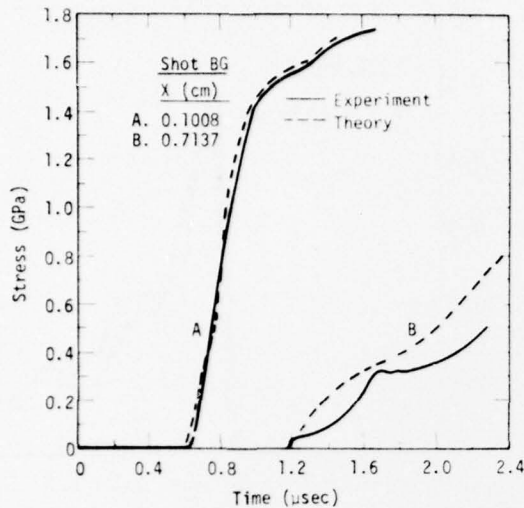


Fig. 12. Comparison of measured and computed transmitted compressive wave profiles for sintered porous Be. Impactor-target geometry used in this shot (shot BG) is also shown. (See Table 4 for details.)

a finite thickness of the gage it takes a nonzero "ring-up" time to bring its stress to that of the surrounding material. The computer calculations give the ring-up time as about $0.15 \mu\text{s}$ or less, which is consistent with most of the experimental profiles. However, the experimental ring-up time may become even larger than the computer prediction under some circumstances.¹⁸ For example, the carbon-Kapton gages were found to respond particularly slowly ($0.5 \mu\text{s}$) at stress $\leq 0.5 \text{ GPa}$ in a test series in (solid) fused quartz. Ring-up time and such delayed response

are likely causes of the slow risetimes in the experimental wave profiles of shots BT-B (Fig. 10(d)) and BR-C (Fig. 11(e)).

It is important to note that a ramped character in the compressive portion of the computed full wave profiles (Figs. 6, 8(c), 9, 10(d)) was formed not just by the dynamic (τ -dependent) effect of the pore closure alone, but, as described above, nonzero gage ring-up time would have also

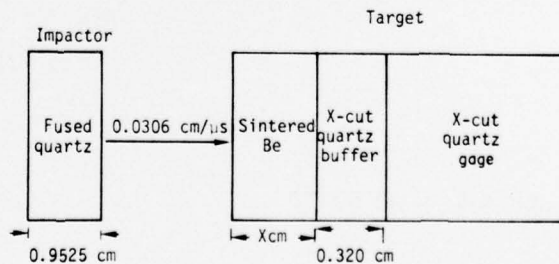
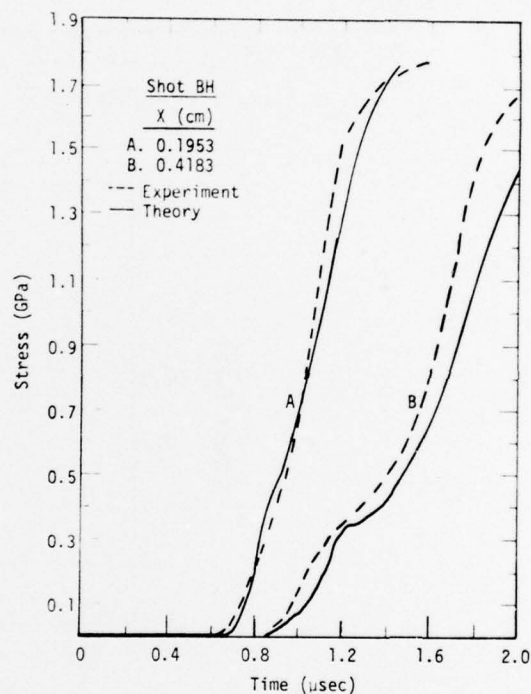


Fig. 13. Comparison of measured and computed transmitted compressive wave profiles for sintered porous Be. Impactor-target geometry used in this shot (shot BH) is also shown. (See Table 4 for details.)

contributed to shape such profiles. This remark is based on our experience that the change of τ alone, no matter how large, is not sufficient to reproduce experimental compressive profiles. For example, a choice of τ which gave a good agreement at the upper portion of the wave fronts gave a poor wave shape at the foot of the wave fronts.

It is interesting to note that the computed wave profiles can reproduce qualitatively small bumps and humps atop the peak stress levels in Figs. 6 and 9. Careful examination of the wave propagation at discrete time intervals has shown that these minor stress changes resulted from an impedance mismatch at the gage-specimen interface. A small, early-arriving portion of the shock is reflected back as a release wave as the gage is ringing up to a peak stress level. The newly created release wave interacts with the oncoming main shock, reducing the latter's stress. For a thin porous Be specimen, the release wave can even reach the impact surface and, upon reflection, create small compressive waves as seen in Figs. 6 and 9. Disagreement between the measured and the predicted profiles for waves propagated over long distances, e.g. shots BS-B (Fig. 7(d)) and BU-D (Fig. 8(f)), originates partly from the use of 0.1 GPa to describe an "average" behavior of the yield stress over the entire stress range considered here. This oversimplification most affected those cases where stress pulses propagated over considerable distances (~ 1.9 cm), and underwent an appreciable amount of attenuation from the peak levels (1.4 and 0.7 GPa, respectively). The observed disagreement (~ 0.1 GPa) could have been reduced with

more refinement of the model parameters at low stress levels below about 0.2 GPa. A more important source of the disagreement, however, occurs from release waves that were created at the circumference of the target assembly. These waves had enough time to reach the gage locations and interfered destructively with the oncoming compressive waves. Analysis of shots BS-B and BU-D with a one-dimensional hydrodynamic code is therefore not well justified.

In Fig. 14, two computed wave profiles corresponding to shot BR-D (Fig. 11(f)) are superimposed along with the experimental wave profile. One of the computed profiles was obtained including the gage in the calculation, while the other was taken at the same position but without the gage. The importance of including the gage in a numerical wave-propagation calculation shows up rather clearly in this example. First, as might have been expected from the finite ring-up time discussed earlier, the presence of the gage reduces the peak stress of an attenuated wave, by about 0.03 GPa in this case. The result will be substantially increased predicted attenuation. Second, the gage tends to smooth out the rather pronounced release characteristics that are calculated for the case without the gage. This release behavior gives a false impression that the material seems to be "suddenly" slowing down the release wave. As is clear from Fig. 14, this is, of course, not true; rather, the behavior is due to a time delay for the gage to "ring down," a process opposite to the ring-up process discussed earlier.

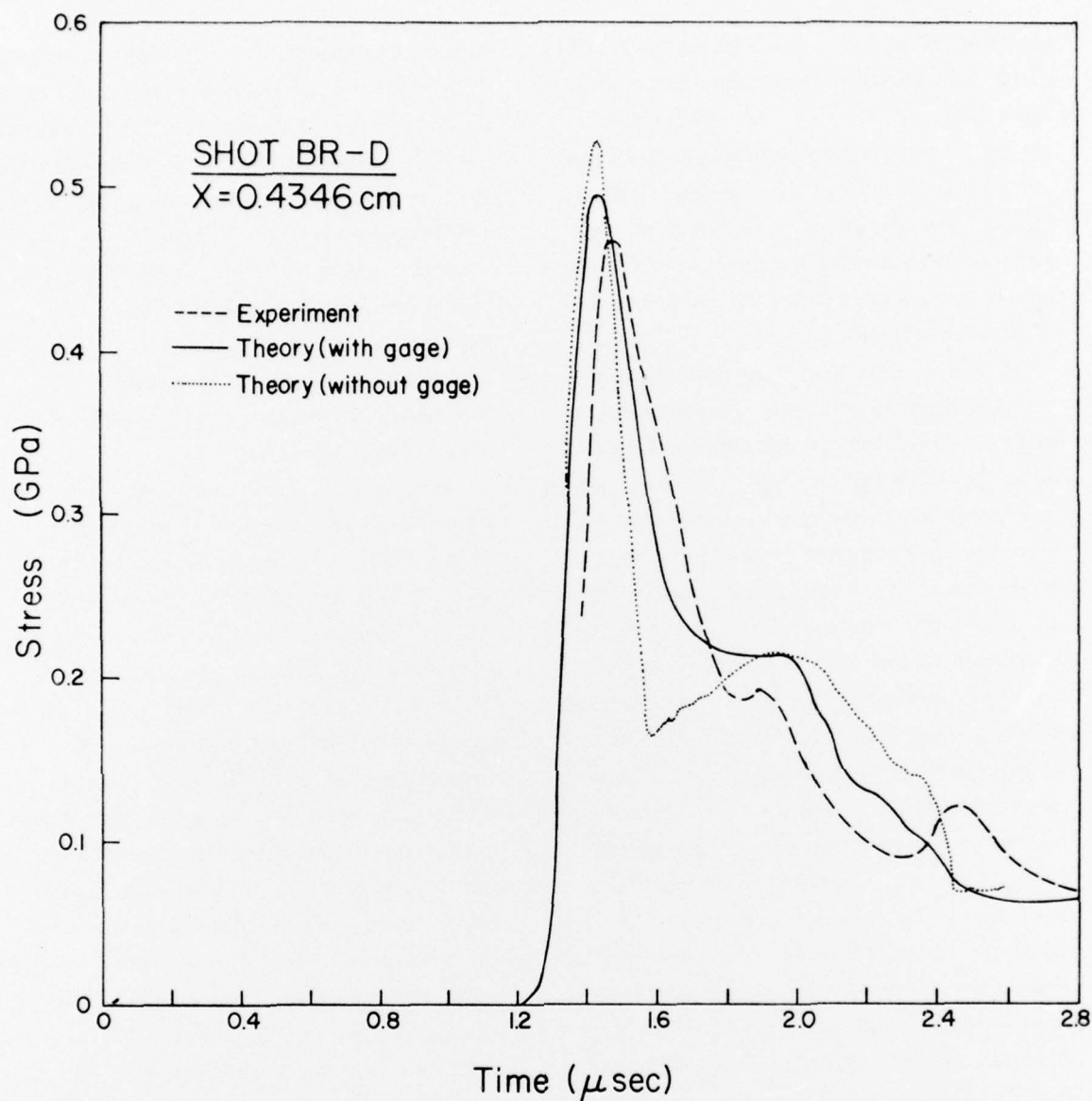


Fig. 14. Comparison of measured (dashed line) and two computed wave profiles for shot BR-D (sintered porous Be): solid line is computed profile with the carbon-Kapton gage, and dotted line is computed profile without the gage. (See Table 5 for experimental parameters.)

5.3 RELEASE WAVE

The attractiveness of the model shows up more distinctly along the release wave path. In contrast to the earlier (hydrodynamic) models, the present model is an

elastic-plastic model. Hence, the experimental release wave velocity, which lies close to the longitudinal sound speed, can be successfully reproduced in the model calculation (Figs. 6-11). Both the agreement in the arrival times of the release

waves and the general shapes of attenuated wave profiles are satisfactory.

There is a tendency for the computed release wave profiles, after arriving at correct times at the gages, to release slightly too fast in later portions of the release profile. This can be seen in Figs. 6, 8(e), 9, and 10(d). This discrepancy may originate from (i) inaccurate release behavior in the model, (ii) erroneous EOS parameters for the gage, and (iii) hysteresis in the gage. Inaccuracy in the model probably did not introduce a significant error, since arrival times of the release wave were accurately predicted from the model. On the other hand, we observed earlier that the release profiles of shot BR-D (Fig. 14) are affected sensitively by the EOS of the carbon-Kapton gage. This is also very likely true in the cases considered here. Therefore, a refined EOS of the gage would likely bring the measured and the calculated release profiles closer. Another source for the observed deviation is the possibility of gage hysteresis, resulting in different resistance-stress calibration scales along the compressive and the release portions of the stress path.¹⁸

Figures 10 and 11 exhibit a complex release behavior for the as-sprayed specimen. Examination of the corresponding model calculations shows that the release of a propagating wave occurs, crudely speaking, in a stairstep manner; i.e., elastic release of an initial peak stress to a level calculated from the von Mises yield condition, further elastic release of the second stress level to the third stress level specified by the yield condition, and so on. Actually, the computed wave profiles look more complicated than this,

since the newly created waves are traveling at different speeds, and wave interactions occur among such waves as well as among these waves and waves reflected from the impact surface and from the discontinuities at the gages. It is interesting to note that this behavior observed for the as-sprayed specimen does not apparently occur (or is very small) in the observed and computed profiles of the sintered specimen (Figs. 7(c), 8(d), and 8(e)). Since the yield stress (0.1 GPa) used for the sintered specimen is relatively small over most stress ranges considered here, and the release velocities at different stress levels are nearly equal (~ 1.2 cm/ μ s), both the widths and the amplitudes of elastic waves which might be generated along the release portion of the wave are small and are smoothed out very rapidly by the wave interactions.

5.4 OTHER REMARKS

Rather than examining a stress history recorded at a fixed carbon-Kapton gage station, various processes discussed above can be seen better by viewing a series of "snapshots" of the wave profiles taken at different instants of time.

Figure 15 gives these snapshots corresponding to shot BT-E (Fig. 10(g)). Both the elastic-plastic character of the release wave and the effect of the carbon-Kapton gage can be seen clearly here. Separation of specimen and impactor occurs at the impact surface when the release wave from the back surface of the PMMA impactor starts to propagate inside the porous specimen. The computer-generated wave profile is compared with the corresponding experimental profile in Fig. 15(f).

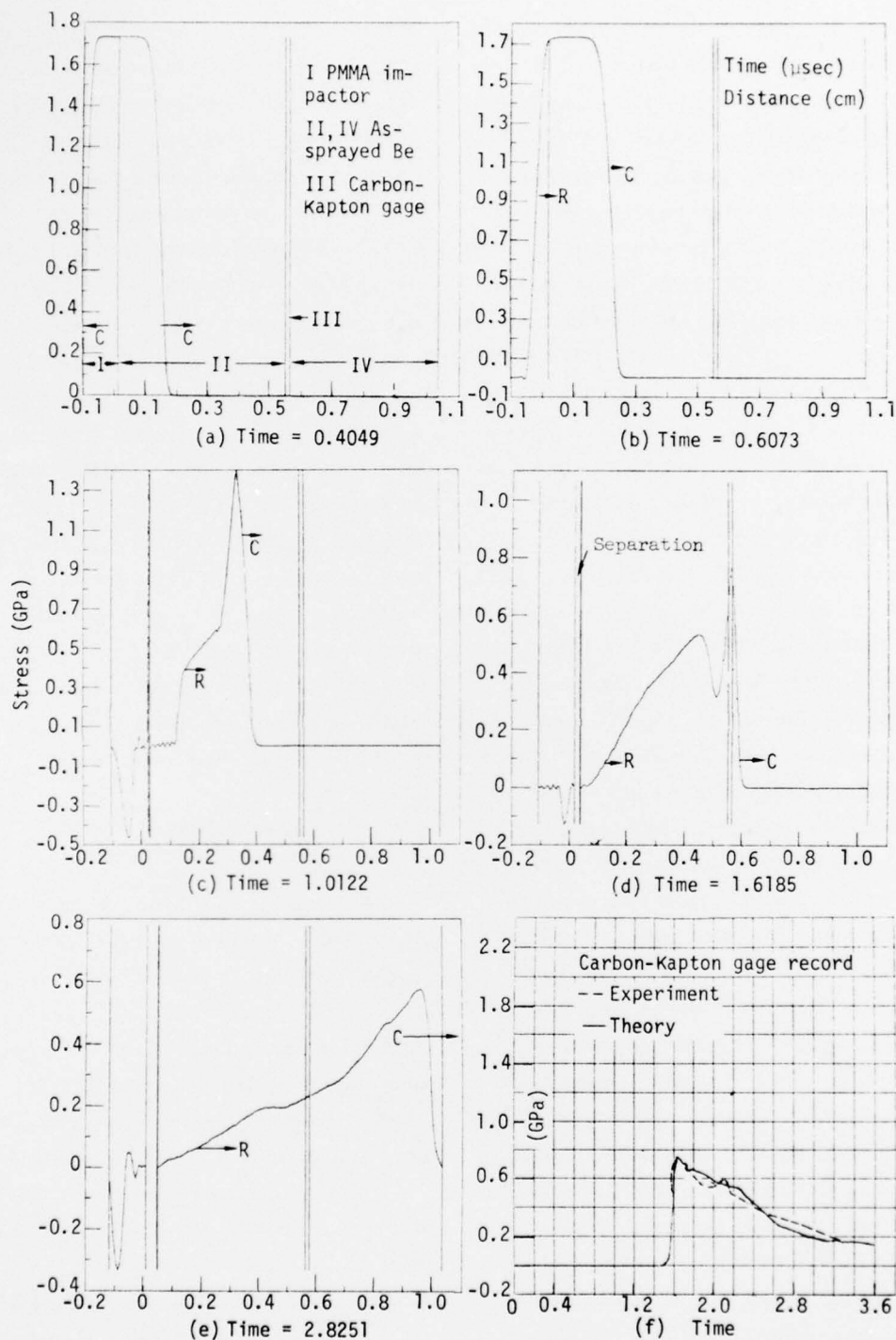


Fig. 15. Snapshot of stress waves generated from impacting a PMMA plate onto an as-sprayed porous beryllium target at impact velocity of $0.0750 \text{ cm}/\mu\text{s}$. Stress history obtained at carbon-Kapton gage is shown in (f). Dashed line is experimental profile. This shot corresponds to shot BT-E. (See Table 5 and Fig. 10(g).)

Similar snapshots for the porosity parameter α are shown in Fig. 16. We note a large plastic change in α after the passage of the wave train. As shown in Fig. 10(f), this change occurs because the loading and unloading paths are completely different. Nevertheless, an appreciable amount of pore space is re-opened. This is shown in Fig. 16(c).

It is easy to show this from Eqs. (8) and (10a). Integrating Eq. (8) under the assumption of $K_s \gg \alpha P$ (which is true in this case since $K_s = 155.6$ GPa and $P \leq 3$ GPa) gives

$$\alpha = \alpha_\infty / \left\{ 1 - \frac{(\alpha_1 - \alpha_\infty)}{\alpha_1} \exp[A(P_1 - P)] \right\}, \quad (17)$$

where P_1 and α_1 are the values of P and α at the initial release point, and

$$A \equiv (1/K_0 - \alpha_0/K_s) \alpha_\infty / (\alpha_0 - \alpha_\infty). \quad (18)$$

For example, release from $P = 1.2$ GPa under static loading to zero pressure changes α by an insignificant amount (from 1.069 to 1.071) for the sintered specimen ($\alpha_0 = 1.1254$) but by about 2% (from 1.068 to 1.090) in the case of the as-sprayed specimen ($\alpha_0 = 1.163$).

The calculated impact surface record on shot BT-A (Fig. 10(c)) shows an overshoot at the shock front. Although a similar structure was not found in the corresponding experimental record (possibly because of the gage ring-up effect discussed earlier), there are other experimental records that show signs of such an overshoot. Two such experimental records are shown in Fig. 17, where a sintered Be impactor collides with a buffered x-cut quartz target, with stress records taken at 0.32 cm from the impact

surface. Unfortunately the tests shown here had both tilt and electrical breakdown. Figure 17(a) corresponds to our model calculation of shot BE (Fig. 17(c)) using several different values of τ . These are profiles computed not at the gage location but at the impact surface. Other additional model calculations have shown that this is a surface phenomenon; i.e., the overshoot can be observed only at or near the impact surface and, at even small distances into the material (< 0.1 cm), attenuation has removed the overshoot from the wave front. It is easy to see from the dynamic path shown in Fig. 5(b) that such a surface phenomenon can be expected from the present model. The stress at the impact surface overshoots because the stress pulse is sharply rising and the risetime of the shock is much smaller than the response time (τ) of the pore closure. It is also noteworthy that the overshoot is higher at higher stress levels (shot BT-A in Fig. 10(c) and shot BE in Fig. 17) and may even disappear at sufficiently low stresses (shot BR-A in Fig. 11(c)). It should be emphasized here that the experimental data presented in Fig. 17 are relatively poor in quality, so that any conclusion based on them should be considered to be tentative until more accurate data become available. A precise measurement of wave profiles at the impact surface would be useful, since the decay time of the overshoot can be related to τ (Fig. 17(a)). For such experiments, the porous Be specimens must be carefully prepared so that the surface layers of the specimens are exceptionally flat and smooth, since the overshoot is of such short duration ($\leq 0.04 \mu s$) and tilt or

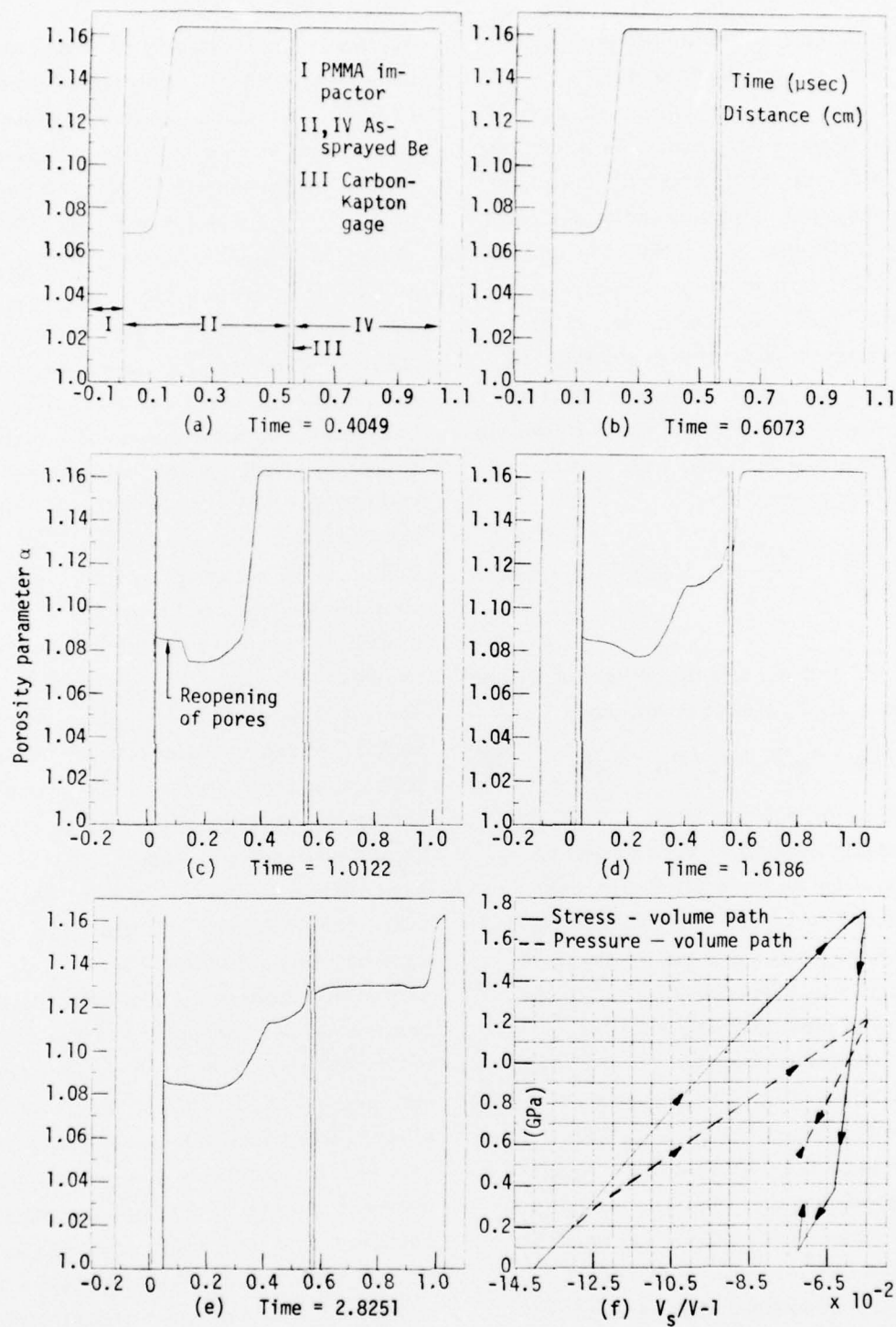
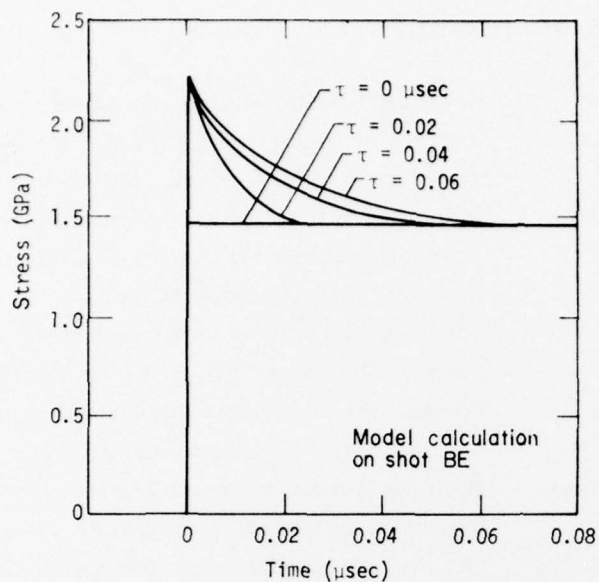
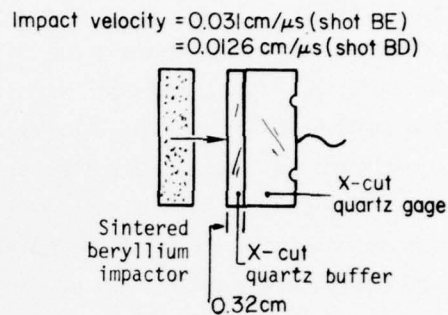


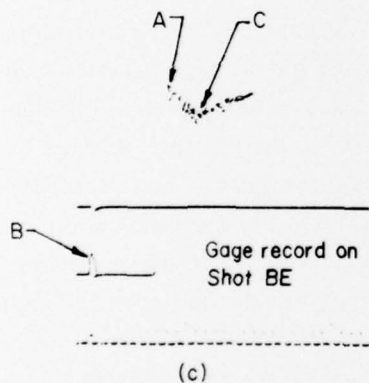
Fig. 16. Snapshots of the porosity parameter for the same impactor-target geometry as used in Fig. 15; (f) shows stress- and pressure-vs-strain paths taken during the passage of the wave train by Lagrangian element which was initially at 0.139 cm from the impact surface.



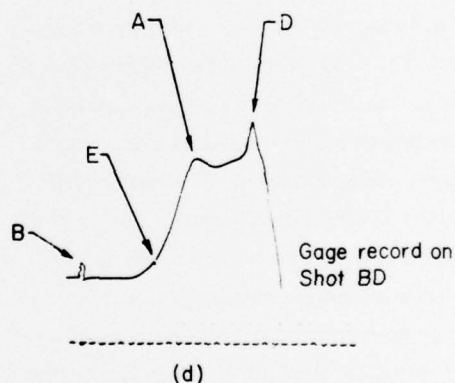
(a)



(b)



(c)



(d)

Fig. 17. Stress histories of sintered porous Be: (a) the computed profile (shot BE) at the impact surface with different values of τ , (b) impactor-target geometry for shots BE and BD, (c) experimental profile (shot BE) measured at 0.32 cm behind the impact surface, and (d) experimental profile (shot BD) measured at the same position as (c) but at a slower impactor speed. A = overshoot, B = time of impact, C = stress-induced electrical breakdown, D = reflection of wave from back of gage, and E = impactor tilt effect.

electrical noise can easily mask the effect. The plate-impact geometry of Fig. 17(b) would be adequate for this purpose, but a much thinner buffer than the ones used in

the present tests would be desirable so that any possible attenuation of the overshoot during the propagation through the buffer can be minimized.

6. Conclusions

In summary, we have shown that the present model can describe wave propagation in both sintered and as-sprayed porous beryllium layers within the necessary accuracy. Both the compressive characteristics (first-wave arrival time, risetime of shock, and peak stress) and the release characteristics (arrival time of release wave and general attenuated wave shape) of shocks have been reproduced satisfactorily for different stresses and pulse durations as well as for different thicknesses of the porous specimens. Slight deviations between the experimental and computed wave profiles lie mostly within the combined errors of the model and the experimental data. We have also shown that the elastic-plastic effect plays a major role in shaping the wave profiles, and that release wave profiles recorded at the carbon-Kapton gage depend significantly on the EOS of the gage. The model also predicts an interesting effect that impact surface measurements could produce, i.e., an overshoot in the compressive wave profile beyond a certain stress level.

Important assumptions in the present model are: (i) isotropy of the medium, (ii) porosity change directly attributable to the pressure, (iii) separability of the

pressure and the deviatoric stress as expressed by Eq. (11), and (iv) a negligible Bauschinger effect. While the isotropy assumption (i) is not strictly correct at lower stresses (≤ 1 GPa), no theoretical analysis on the anisotropic contribution to wave profiles has been made. Similarly, there are presently no theoretical or experimental studies as to the validity of assumptions (ii)-(iv). The good agreement presented here suggests that these assumptions might be reasonable ones to use for the wave propagation study.

Finally, both the experimental and the theoretical analyses presented here suggest different yield behavior for the sintered and plasma-sprayed specimens. The results on the 1-D experiments and the Hugoniot data do not agree with each other for sintered beryllium. Before attributing this disagreement to the rate-dependent effect in the Hugoniot data, careful dynamic and static experiments should be performed to find out any other source of the difference. Future work could be concerned with the effects of varying amounts of porosity, and with the sintering conditions as they affect the tradeoff between material strength and its ability to attenuate a short-duration shock pulse.

Acknowledgments

We are grateful to T. Lundeen, J. French, J. Woodruff, and J. Stanley for computational support, to W. H. Gust, H. E. Hanafey, E. O. Snell, R. N. Schock, A. Abey, A. Duba, and

D. R. Green for experimental support, and to A. C. Holt, M. M. Carroll, O. Walton, and M. van Thiel for continued useful advice during the progress of this work.

References

1. B. M. Butcher, J. Appl. Phys. **44**, 4576 (1973).
2. B. M. Butcher, M. M. Carroll, and A. C. Holt, J. Appl. Phys. **45**, 3864 (1974).
3. W. M. Isbell and R. R. Horning, Behavior of Porous Beryllium Under Thermo-mechanical Loading: Part 3. Shock Wave Studies, Lawrence Livermore Laboratory Rept. UCRL-51682-3 (1974).
4. J. E. Hanafee and E. O. Snell, Behavior of Porous Beryllium Under Thermo-mechanical Loading: Part 6. Effect of Pressure on the Microstructure of Plasma-Sprayed Beryllium, Lawrence Livermore Laboratory Rept. UCRL-51682-6 (1974).
5. R. N. Schock, A. E. Abey, and A. G. Duba, Behavior of Porous Beryllium Under Thermomechanical Loading: Part 2. Quasi-Static Deformation, Lawrence Livermore Laboratory Rept. UCRL-51682-2 (1974).
6. Ultrasonic data provided by D. R. Green of LLL (private communication).
7. Hugoniot data points to 33.5 GPa provided by W. H. Gust of LLL (private communication).
8. A. C. Holt, A. S. Kusubov, D. A. Young, and W. H. Gust, Thermomechanical Response of Porous Carbon, Lawrence Livermore Laboratory Rept. UCRL-51330 (1973).
9. W. Herrmann, J. Appl. Phys. **40**, 2490 (1969).
10. J. K. Mackenzie, Proc. Phys. Soc. **B63**, 2 (1950).
11. L. Seaman, Porholt, a Rate-Dependent Constitutive Relation for Porous Materials, Stanford Research Institute, Poulter Laboratory Technical Rept. 001-73 (Feb. 1973).
12. N. Cristescu, Dynamic Plasticity (North-Holland, Amsterdam, 1967), p. 561.
13. A. C. Holt, M. M. Carroll, and B. M. Butcher, Proceedings of the RILEM-IUPAC International Symposium, Prague, Sept. 18-21, 1973.
14. F. H. Ree, A Computer Model for Wave Propagation in Porous Materials, Lawrence Livermore Laboratory Rept. UCRL-51673 (1974).
15. M. L. Wilkins, Calculation of Elastic-Plastic Flow, Lawrence Livermore Laboratory Rept. UCRL-7322 (1969).
16. The hydrostat used here was provided for us by R. Schock et al. of LLL. This hydrostat, which was obtained without cyclic loading, and the multiply cycled hydrostat in Ref. 5 agree closely.
17. D. Christman and F. Feistman, Dynamic Behavior of S-200-E Beryllium, General Motors Technical Center, Warren, Michigan, Rept. MSL-71-23 (DNA-2785F) (Feb. 1972).
18. R. R. Horning and W. M. Isbell, Behavior of Porous Beryllium Under Thermo-mechanical Loading: Part 7. Calibration Studies on the Carbon Piezoresistive Gage, Lawrence Livermore Laboratory Rept. UCRL-51682-7 (1974).

19. M. M. Carroll and A. C. Holt, J. Appl. Phys. 43, 759 (1972).
20. M. M. Carroll and A. C. Holt, J. Appl. Phys. 43, 1626 (1972).
21. F. E. Prieto and C. Renero, J. Appl. Phys. 44, 4013 (1973).
22. The iterative algorithm described here was developed by T. Lundeen at LLL.
23. M. Barker and R. E. Hollenbach, J. Appl. Phys. 41, 4208 (1970).
24. R. S. Hawke et al., J. Appl. Phys. 43, 2734 (1972).
25. The value $\gamma = 0.0752$ for fused quartz was chosen by M. Kamegai of LLL by comparing various γ 's listed in the literature (private communication).
26. R. A. Graham, Phys. Rev. B 6, 4779 (1972).
27. E. B. Royce, GRAY, a Three-Phase Equation of State for Metals, Lawrence Livermore Laboratory Rept. UCRL-51121 (1971).

RERUN - 3/11/75
W.M. ISBELL - 2 25